Heterogeneity and anisotropy of the lithosphere of SE Tibet from surface wave array tomography

Huajian Yao, Robert D. van Der Hilst, Jean-Paul Montagner

Heterogeneity and anisotropy of the lithosphere of SE Tibet from surface wave array tomography

Huajian Yao,[1,2] Robert D. van der Hilst,[1] and Jean-Paul Montagner[3]

Received 17 November 2009; revised 17 May 2010; accepted 23 June 2010; published 3 December 2010.

[1] Understanding the geotectonic evolution of the southeastern Tibetan plateau requires knowledge about the structure of the lithosphere. Using data from 77 broadband stations in SW China, we invert Rayleigh wave phase velocity dispersion curves from ambient noise interferometry (T = 10–40 s) and teleseismic surface waves (T = 20–150 s) for 3-D heterogeneity and azimuthal anisotropy in the lithosphere to ~150 km depth. Our surface wave array tomography reveals (1) deep crustal zones of anomalously low shear wave speed and (2) substantial variations with depth of the pattern of azimuthal anisotropy. Upper crustal azimuthal anisotropy reveals a curvilinear pattern around the eastern Himalayan syntaxis, with fast directions generally parallel to the main strike slip faults. The mantle pattern of azimuthal anisotropy is different from that in the crust and varies from north to south. The tomographically inferred 3-D variation in azimuthal anisotropy helps constrain the source region of shear wave splitting. South of ~26°N (off the high plateau) most of the observed splitting can be accounted for by upper mantle anisotropy, but for stations on the plateau proper (with thick crust) crustal anisotropy cannot be ignored. On long wavelengths, the pattern of azimuthal anisotropy in the crust differs from that in the mantle. This is easiest explained if deformation varies with depth. The deep crustal zones of low shear wave speed (and, presumably, mechanical strength) may represent loci of ductile deformation. But their lateral variation suggests that in SE Tibet (localized) crustal channel flow and motion along the major strike slip faults are both important.

Citation: Yao, H., R. D. van der Hilst, and J.-P. Montagner (2010), Heterogeneity and anisotropy of the lithosphere of SE Tibet from surface wave array tomography, *J. Geophys. Res.*, *115*, B12307, doi:10.1029/2009JB007142.

1. Introduction

[2] Ever since the pioneering work by Argand some 90 years ago [*Argand*, 1924], the Eocene formation and subsequent geological evolution of the Tibetan plateau in response to India-Eurasia plate convergence have been the focus of much geological and geophysical research (for reviews, see *Molnar et al.* [1993], *Yin and Harrison* [2000], *Tapponnier et al.* [2001], *DeCelles et al.* [2002], and *Royden et al.* [2008]). The mechanism of plateau formation and regional deformation is still debated, with rigid block extrusion [*Tapponnier et al.*, 1982, 2001], distributed crustal thickening [*England and Houseman*, 1986], injection of Indian crust into Tibetan lower crust [*Zhao and Morgan*, 1987], and crustal channel flow [*Royden et al.*, 1997; *Beaumont et al.*, 2001] representing popular end-members.

[3] Our study region in SW China encompasses the southeastern margin of the Tibetan plateau and the so-called "indenter corner" between the eastern Himalayan syntaxis (EHS) and Sichuan basin, a mechanically rigid part of the Yangtze or South China craton. This area is of significant societal and academic interest because of the high level of seismicity and because of the opportunities it offers to study the mechanisms for the buildup and eastward expansion of the Tibetan plateau. Tectonic deformation in this southern extremity of the trans-China seismic belt is often accompanied by large earthquakes, mostly along the major strike slip faults (such as the Xianshuihe-Xiaojiang faults) and (less frequently) along (reactivated) thrust belts, such as the devastating 12 May 2008 Wenchuan earthquake along the Longmen Shan fault zone [*Burchfiel et al.*, 2008; *Hubbard and Shaw*, 2008; *Liu-Zeng et al.*, 2009]. Deformation in this region is influenced by northward subduction of the Indian lithosphere [*Yin and Harrison*, 2000; *Li et al.*, 2008], eastward subduction of the Burmese microplate along the Burma arc [*Ni et al.*, 1989; *Huang and Zhao*, 2006; *Li et al.*,

[1]Department of Earth, Atmospheric, and Planetary Sciences, Massachusetts Institute of Technology, Cambridge, Massachusetts, USA.
[2]Now at Institute of Geophysics and Planetary Physics, Scripps Institution of Oceanography, University of California, San Diego, La Jolla, California, USA.
[3]Seismology Laboratory, Institut de Physique du Globe de Paris, Paris, France.

0148-0227/10/2009JB007142

2008], resistance to further eastward expansion of the Tibetan plateau by Sichuan basin [*Cook and Royden*, 2008], and, probably, by upper mantle processes related to subduction much further to the southeast [*Replumaz et al.*, 2004; *Royden et al.*, 2008; *Li and van der Hilst*, 2010]. The crust between EHS and Sichuan basin has undergone clockwise deformation around the EHS [*Zhang et al.*, 2004; *Shen et al.*, 2005], but the mechanisms for deformation are not yet well understood.

[4] Geological studies suggest that in the past 15 Ma uplift of the eastern part of the Tibetan plateau has occurred with relatively little crustal shortening or eastward motion of the deformation front (for a recent review, see *Royden et al.* [2008]). Along with the regional topographic gradients, this has been explained by influx of crustal material from the central plateau through ductile channel flow in the deep crust [*Royden et al.*, 1997; *Clark and Royden*, 2000; *Shen et al.*, 2001; *Cook and Royden*, 2008]. However, the occurrence and importance of such crustal flow has been the subject of heated debate.

[5] Several geophysical observations support the possibility of crustal flow. Seismic and magnetotelluric surveys suggest the presence of partial melt and reduced viscosity in the middle crust of southern Tibet [*Nelson et al.*, 1996; *Unsworth et al.*, 2005] and thermomechanical channel flow in a weak middle crust was proposed to explain the Himalayan-Tibetan tectonics [*Beaumont et al.*, 2001, 2004]. Strong radial anisotropy [*Shapiro et al.*, 2004] and near-horizontal rock fabric [*Ozacar and Zandt*, 2004] in the Tibetan middle-to-lower crust also suggest midlower crustal material flow beneath the Tibetan plateau. For the southeastern margin of the Tibetan plateau, both surface wave array tomography [*Yao et al.*, 2008; *Li et al.*, 2009], body wave tomography [*Huang et al.*, 2002; *Wang et al.*, 2003; *Huang et al.*, 2009], and receiver function analyses [*Hu et al.*, 2005; *Xu et al.*, 2007; *Liu et al.*, 2009; *Zhang et al.*, 2009; *Wang et al.*, 2010] reveal widespread zones of low (shear) wave speed at midcrustal or lower-crustal depth, and magnetotelluric profiling [*Bai et al.*, 2010; *Rippe and Unsworth*, 2010] has detected zones of reduced resistivity in the middle/lower crust. The reduced shear wave speed and (electrical) resistivity may have a common cause in the form of aqueous melts, which is consistent with the high geotherm in SE Tibet [*Hu et al.*, 2000] and which would facilitate ductile flow. Gravity anomalies indicate very weak lithosphere in the region from central Tibet to SW China [*Jordan and Watts*, 2005].

[6] The case for channel flow beneath eastern Tibet is not straightforward, however. On the one hand, uninterrupted flow over large distances is not easily reconciled with the strong lateral heterogeneity of the low shear speed zones revealed by surface wave array tomography [*Yao et al.*, 2008] and receiver functions [*Xu et al.*, 2007; *Wang et al.*, 2010], unless, of course, flow occurs also in parts of the crust outside the zones of extreme wave speed or in the shallow mantle (or both). On the other hand, some studies have argued for vertically coherent deformation between crust and mantle [e.g., *Flesch et al.*, 2005], which, if true, may be difficult to achieve if the viscosity of the middle or lower crust is several orders magnitude less than that of the upper rigid crust (as proposed in the flow models of *Royden et al.* [1997] and *Clark and Royden* [2000]). The level (and lateral extent) of mechanical coupling or decoupling is not yet well known, however.

[7] Joint analysis of GPS, surface geology, and shear wave splitting measurements has been used to argue for vertically coherent deformation in the crust and upper mantle in Tibet but decoupling beneath Yunnan, SW China [*Flesch et al.*, 2005]. Using shear wave splitting observations, *Lev et al.* [2006] also argue for crust-mantle decoupling beneath Yunnan, but they cannot constrain the level of coupling beneath the plateau proper. On the basis of shear wave splitting and the surface strain field from GPS data, *Sol et al.* [2007] argue for mechanical coupling across the crust-mantle interface beneath much of SE Tibet (except Yunnan), and *Wang et al.* [2008] argue for crust-mantle coupling in Tibet and surrounding regions (including Yunnan) from joint analysis of more shear wave splitting measurements and GPS observations.

[8] It is important to realize that these interpretations of shear wave splitting and GPS data rely on assumptions about the origin of seismic anisotropy and the relationship between this anisotropy and the GPS data. Under the assumption that observed shear wave splitting is produced by (azimuthal) anisotropy in the upper mantle, the congruity of splitting orientations and crustal structure or strain inferred from GPS has been used to suggest coherent crust-mantle deformation. The depth of the anisotropy that causes shear wave splitting is, however, not well known because the observed splitting represents the integrated effect of anisotropy along steep raypaths [e.g., *Savage*, 1999]. Furthermore, comparing GPS data with strain induced anisotropy is not straightforward: (1) the GPS surface velocity field depends on the geographical reference frame, whereas strain does not; (2) the strain rate derived from the spatial gradient of the velocity field reflects the present-day (instantaneous) rate of surface deformation, whereas seismic anisotropy is influenced by (finite) strain history; and (3) without geodynamical modeling the GPS observations (velocity or strain rate) provide little insight about deformation in the deeper crust. Thus, inferences about crust and mantle deformation (e.g., coupling or decoupling) from comparison of the instantaneous surface strain rate field from GPS and shear wave splitting data have considerable uncertainty, especially in regions with a complicated deformation history and thick and highly deformed crust, such as the Tibetan plateau.

[9] Knowing how the azimuthal anisotropy that produces shear wave splitting varies with depth would greatly help us understand the deformation of crust and upper mantle. Surface wave tomography has been used to constrain upper mantle shear velocity heterogeneity and azimuthal anisotropy on regional scales [e.g., *Griot et al.*, 1998b; *Simons et al.*, 2002], but to resolve crustal structure we need measurements at shorter periods than used in those studies. We follow *Yao et al.* [2006, 2008] and combine short-period phase velocity dispersion measurements from ambient noise interferometry with longer period data from two-station analysis. We present 3-D models of the heterogeneity and azimuthal anisotropy of the lithosphere beneath the southeastern part of the Tibetan plateau (including western Sichuan and northern Yunnan of SW China) and compare

the anisotropy thus derived with shear wave splitting measurements. The main questions we aim to address are as follows: (1) Can this surface wave data resolve 3-D heterogeneity and (azimuthal) anisotropy in the crust and uppermost mantle? (2) How does the tomographically inferred 3-D anisotropy compare with results from shear wave splitting? (3) What are the implications for our understanding of the deformation of SE Tibet?

2. Data and Dispersion Analysis

[10] In 2003 and 2004, MIT, with Chengdu Institute of Geology and Mineral Resources (Sichuan, China), deployed 25 broadband seismograph stations between Sichuan basin and the eastern Himalaya syntaxis (EHS). For the study presented here, we use data from the MIT array along with data from a 50 station (temporary) array deployed in the same period by Lehigh University and permanent stations in Kunming (KMI) and Lhasa (LSA), which are part of the Global Seismographic Network (Figure 1a).

[11] Following *Yao et al.* [2006, 2008], we measure for all station pairs the interstation Rayleigh wave phase velocity dispersion from empirical Green's functions (EGFs), which are constructed from ambient noise correlation of about 1 year data and from traditional two-station (TS) analysis, which uses teleseismic earthquake data. The EGF approach yields measurements for periods T = 10–50 s, which are most sensitive to crustal structure, and the TS method yields measurements for periods T = 20–150 s, which constrain structure in the deep crust and lithospheric mantle.

[12] Measurement from EGFs and the joint interpretation of data measured from EGF and TS analysis should be done with care, and two aspects deserve special attention. First, uneven distribution of ambient noise energy can combine with structural heterogeneity and anisotropy to produce an azimuth-dependent bias of interstation phase velocity measurements from EGFs. Such bias could obstruct inversion for azimuthal anisotropy, but in previous studies we have shown that for the arrays in SE Tibet the effect is negligible if we stack causal and anticausal EGFs from 10 monthlong records [*Yao et al.*, 2009; *Yao and van der Hilst*, 2009].

[13] Second, for the periods they have in common (T = 20–50 s) the phase speeds measured from EGFs generally agree with those from the TS method, but for some paths they appear slightly slower. This can be explained by the different sensitivities to heterogeneity. Our inversions are based on ray theory, in which EGF and TS dispersion are both assumed to be sensitive only to structure along the path between two stations. For EGF this is reasonable, but for the periods considered the interstation phase velocity measurements from TS analysis also sense structure outside the two-station path (Appendix A, Figure A1). If the structure between two stations is slow compared to the broader region sampled by the surface waves used in the TS approach, then ray theory (and EGFs) will yield lower phase velocities than TS. In our study, the distribution of sources (Figure A2a) and the regional variation in propagation speed (Figure A2b) combine to produce a bias on the order of 0.4%–0.8% for some paths (Figure A3). Although this bias is much smaller than the inferred variation of phase velocity (section 3, below) we correct for it in order to suppress effects of crustal thickness variations outside the array area.

[14] This approach to accounting for a finite frequency effect is ad hoc, but not unreasonable since the entire framework for inversion (e.g., the notion of constructing phase velocity maps followed by point-wise inversion for 1-D wave speed profiles, which are then combined into a 3-D model) is based on asymptotic ray theory. Indeed, given the fundamentally asymptotic nature of the inversion a more explicit use of finite frequency kernels would be less meaningful than it might appear. Developing a full-wave approach requires addressing nonlinearity (because the kernels depend on the 3-D variations in model parameters [e.g., *de Hoop et al.*, 2006]) and the fact that EGFs are approximations of real Green's functions (with the success of their reconstruction depending on, for instance, the distribution of ambient noise sources). Since finite frequency kernels depend critically on the measurement [*de Hoop and van der Hilst*, 2005], determining the real sensitivity of EGF derived phase speed to Earth structure is not trivial.]

[15] Figure 2 presents histograms of the difference in interstation dispersion curve from EGF and TS analysis (after the finite frequency correction) for T = 20–50 s. At each period, the mean difference between phase velocities measured from TS and EGFs ($C_{TS} - C_{EGF}$) is almost zero, but the standard error of the difference increases from ~0.05 km/s at T = 20–40 s to 0.08 km/s at T = 50 s. This reflects the difficulty of recovering EGFs from long-period data. Following *Yao et al.* [2008] we average the EGF and TS dispersion data for T = 20–40 s (yielding 2232 dispersion curves). For $T < 20$ s, we take measurements from the EGF analysis, and for $T > 40$ s, we only use measurements from the TS analysis.

[16] We thus obtain 2413 dispersion curves for T = 10–150 s. The number of measurements at each period is shown in Figure 3a and the average phase velocity dispersion curve (representative of the entire region under study) is shown in Figure 3b. The decrease of the number of measurements with increasing period for the EGF analysis is an effect of the far field approximation (which allows us to use a plane wave representation of surface wave propagation); likewise, the decrease in TS measurements results from the requirement that the two stations are at least half wavelength apart [*Yao et al.*, 2006]. Ray path coverage (shown in Figure 4 for T = 30 and 100 s) is excellent.

3. Phase Velocity Maps and Azimuthal Anisotropy

[17] We use the continuous regionalization due to *Montagner* [1986] and the generalized inversion scheme of *Tarantola and Valette* [1982] to invert path averaged phase velocities at each period for 2-D phase velocity variations. Following *Smith and Dahlen* [1973], and ignoring 4ψ terms, we express the local azimuthally varying Rayleigh wave phase velocity $c(\omega, M, \psi)$ at location M for each angular frequency ω and azimuth ψ as

$$c(\omega, M, \psi) = c_0(\omega)[1 + a_0(\omega, M) + a_1(\omega, M)\cos 2\psi + a_2(\omega, M)\sin 2\psi], \quad (1)$$

where $c_0(\omega)$ is the reference phase velocity (usually the average of all observed phase velocities at a certain frequency)

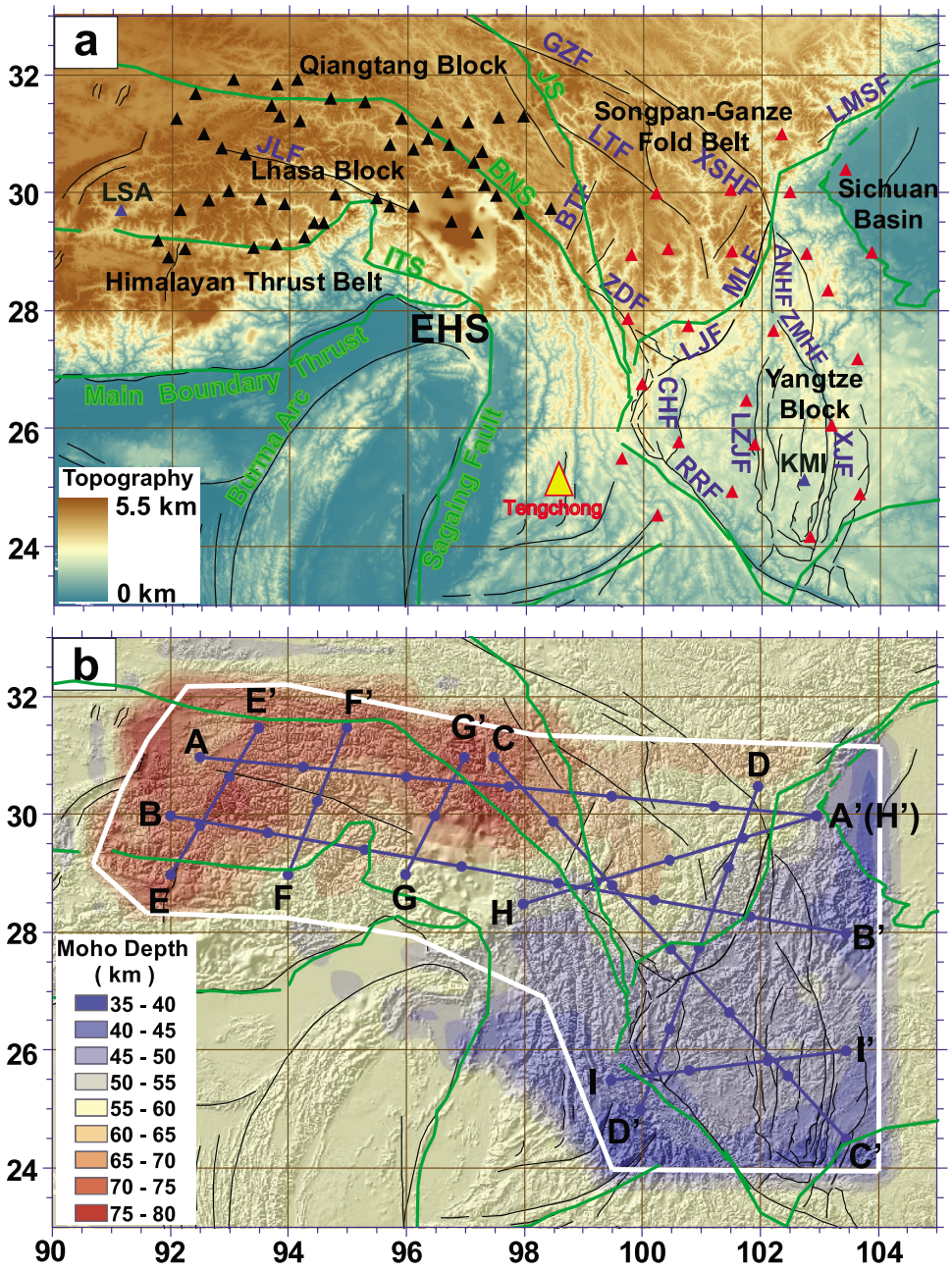

Figure 1. (a) Topography, tectonic elements and fault systems in the southeastern part of the Tibetan plateau around the eastern Himalayan syntaxis (EHS). (b) The depth of Moho discontinuity from surface wave array tomography with reliable results within the region enclosed by the white line. Tectonic boundaries (modified from *Li* [1998] and *Tapponnier et al.* [2001]) are shown as dark green lines and the major faults are depicted with thin black lines [after *Wang et al.*, 1998; *Wang and Burchfiel*, 2000; *Shen et al.*, 2005]. Abbreviations are as follows: JLF, Jiali Fault; GZF, Ganzi Fault; LMSF, Longmenshan Fault; XSHF, Xianshuihe Fault; LTF, Litang Fault; BTF, Batang Fault; ANHF, Anninghe Fault; ZMHF, Zemuhe Fault; ZDF, Zhongdian Fault; LJF, Lijiang Fault; MLF, Muli Fault; CHF, Chenghai Fault; LZJF, Luzhijiang Fault; XJF, Xiaojiang Fault; RRF, Red River Fault; EHS, Eastern Himalaya Syntaxis; JS, Jingsha Suture; BNS, Bangong-Nujiang Suture; ITS, Indus-Tsangpo suture. In Figure 1a, red and black triangles are temporary stations deployed by MIT and Lehigh Univeristy, respectively. The two permanent stations (dark blue triangles) are located at Kunming (KMI) and Lhasa (LSA), China. The Tengchong volcanic area is depicted as the yellow triangle. In Figure 1b, the blue lines show the location of vertical shear wave speed profiles in Figures 9 and 10.

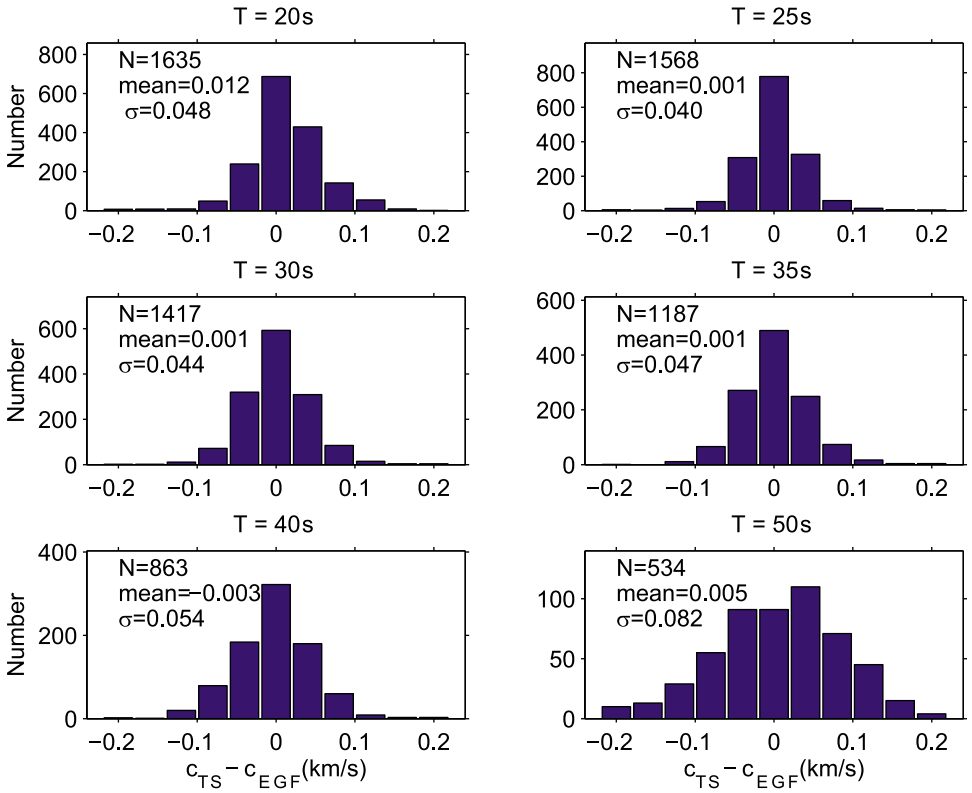

Figure 2. Histogram to show the comparison of interstation Rayleigh wave phase velocity measurements from the EGF analysis and TS analysis (after suppressing the finite frequency effect) at overlapping periods (20–50 s). The horizontal axis show the difference between the phase velocity from the TS analysis (C_{TS}) and that from the EGF analysis (C_{EGF}), i.e., $C_{TS} - C_{EGF}$, while the vertical axis shows the number of interstation paths which falls in the different $C_{TS} - C_{EGF}$ interval each with a width of 0.04 km/s. In each plot, "N" is the total number of paths for comparison and "mean" is the average difference (km/s) of $C_{TS} - C_{EGF}$ for all paths at that period with "σ" the standard deviation (km/s) of the differences in the histogram.

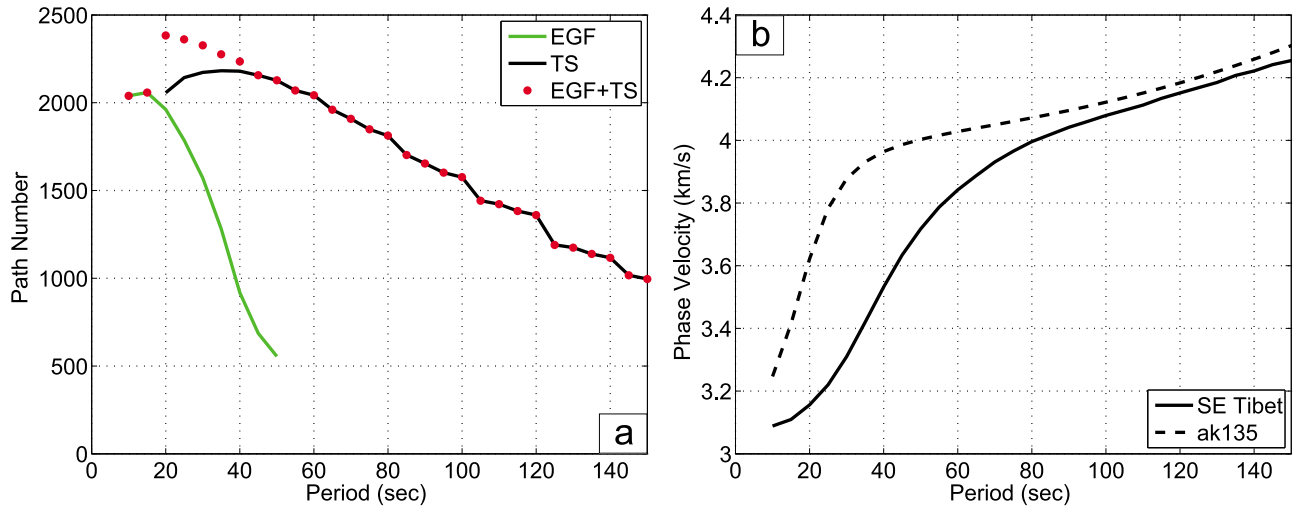

Figure 3. (a) Comparison of the number of interstation phase velocity measurements from EGFs using ambient noise interferometry, TS analysis, and combination of EGF and TS analyses. (b) Average Rayleigh wave phase velocity dispersion curve of SE Tibet (solid line) and that of the *ak135* global 1-D reference model [*Kennett et al.*, 1995] (dashed line).

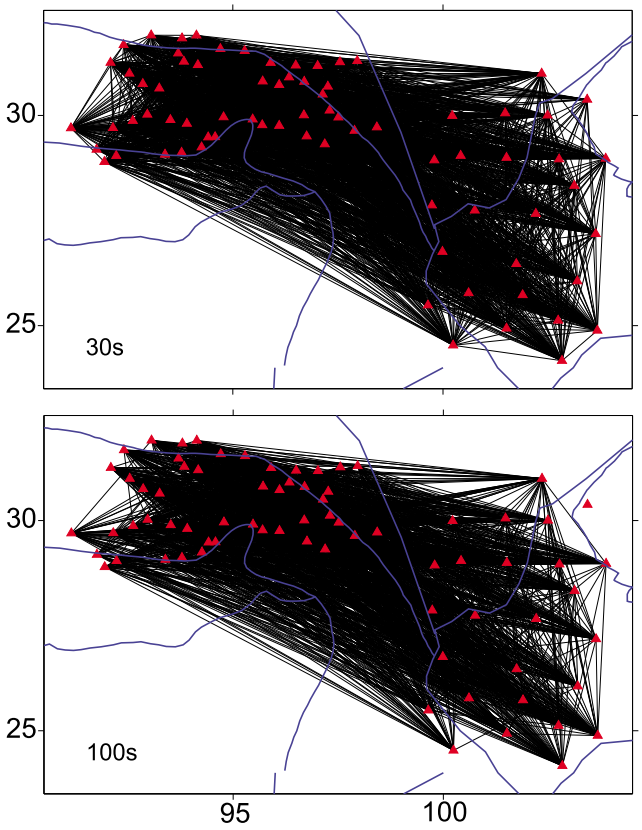

Figure 4. Ray path coverage at 30 and 100 s. The number of raypaths at 30 and 100 s is about 2300 and 1500, respectively.

and a_0 and a_i (with $i = 1, 2$) are the isotropic phase velocity perturbation and the azimuthally anisotropic coefficients, respectively. The inversion for a_i ($i = 0, 1, 2$) is controlled by three parameters: the standard error of phase velocity measurements σ_d, the a priori parameter error σ_p (which constrains the anomaly amplitude), and the spatial correlation length L_c (which constrains the smoothness of the model parameters). Following *Griot et al.* [1998a] and *Simons et al.* [2002], we perform "checker board" resolution tests to determine how well these inversion parameters can be retrieved. The lateral resolution of isotropic phase speed variations is ~100 km (roughly, the average interstation distance) in the array area (Figure 5b). For the azimuthally anisotropic parameters, the lateral resolution reaches ~200 km for $T < 100$ s (Figure 5d). At $T > 100$ s, the azimuthal anisotropy is not well resolved due to relatively poor azimuthal path coverage of measurements at these periods with paths dominated by SSE-NWW direction and because ray theory at long periods (wavelengths > 400 km) may not be valid in a relatively small array region (1300 km × 800 km).

[18] [NB "Checker board" resolution tests only show how well a given inversion algorithm can retrieve structure from a given data set. Their diagnostic value is limited, however, since they assess neither the effect of realistic data quality (systematic errors, for instance, due to off great circle propagation of surface waves for TS analysis, are difficult to simulate) nor the shortcomings of linearization, inadequacies of the theory used for wave propagation (since often the same theory is used for the forward and inverse problem), or the fact that resolution depends on the shape and scale lengths of heterogeneity [*Lévêque et al.*, 1993; *van der Hilst et al.*, 1993]. With these caveats in mind, checker board tests give qualitative information about spatial resolution.]

[19] Our analysis of phase velocity measurements suggests that σ_d is about 1%–2%, and for the inversion we set it to 2% for all measurements. As with regularization, the choice of σ_p and L_c is somewhat subjective; in our study, they are determined empirically from a series of test inversions [*Griot et al.*, 1998a]. For a given a_0, σ_p is set to be twice that of the standard deviation (in percent) of all observed phase velocities at each period with a minimum value of 0.15 km/s. For a_1 and a_2, σ_p is set to be 1.5% of the average phase velocity at each period. The correlation length L_{iso} for the isotropic term is set to be about 100–150 km, determined by the path coverage at each period. In order to obtain robust patterns of azimuthal anisotropy, the correlation length for the azimuthally anisotropic parameters is set to be $2L_{iso}$ at the corresponding period. Similar to the study of the Australian lithosphere [*Simons et al.*, 2002], the tests show that the isotropic part of the solution is insensitive to the choice of the azimuthally anisotropic parameters.

[20] The variation of isotropic phase velocities and azimuthal anisotropy at periods 10, 30, 60, and 100 s are shown in Figure 6. Figure 7 shows that in the array area the posterior errors in the isotropic phase velocity and in the magnitude of azimuthal anisotropy are small compared to the perturbation of phase velocities and the magnitude of azimuthal anisotropy. This demonstrates the reliability of the results (for the periods of interest).

[21] Even without inversion for 3-D structure, we can readily see some interesting features from the isotropic phase velocity and azimuthal anisotropy maps (Figure 6). For example, at $T = 30$ s Rayleigh wave propagation is slow beneath the plateau area and fast beneath the Yangtze block in SW China, which primarily reflects the difference in crustal thickness in this area (see Figure 1b). At $T = 60$ s, low phase velocities are observed along the western margin of Yangtze block, which may indicate that at mantle depths the shear velocity is relatively low around the block boundary. At $T = 10$ s, at which the Rayleigh wave is mostly sensitive to structure between ~5 and 15 km depth, the fast polarization axes of Rayleigh waves reflect a curvilinear pattern around the eastern Himalayan syntaxis that is also conspicuous in the GPS surface velocity field [*Zhang et al.*, 2004]. At $T = 60$ s and $T = 100$ s the fast polarization pattern is different from that at 10 s, giving a first indication that anisotropy in the shallow crust differs from that in the upper mantle.

4. Inversion for Shear Wave Speed and Azimuthal Anisotropy

[22] *Yao et al.* [2008] used the neighborhood algorithm (NA) [*Sambridge*, 1999a, 1999b] to invert for the isotropic wave speed variations. NA is computationally expensive, however, and for the large number of parameters considered

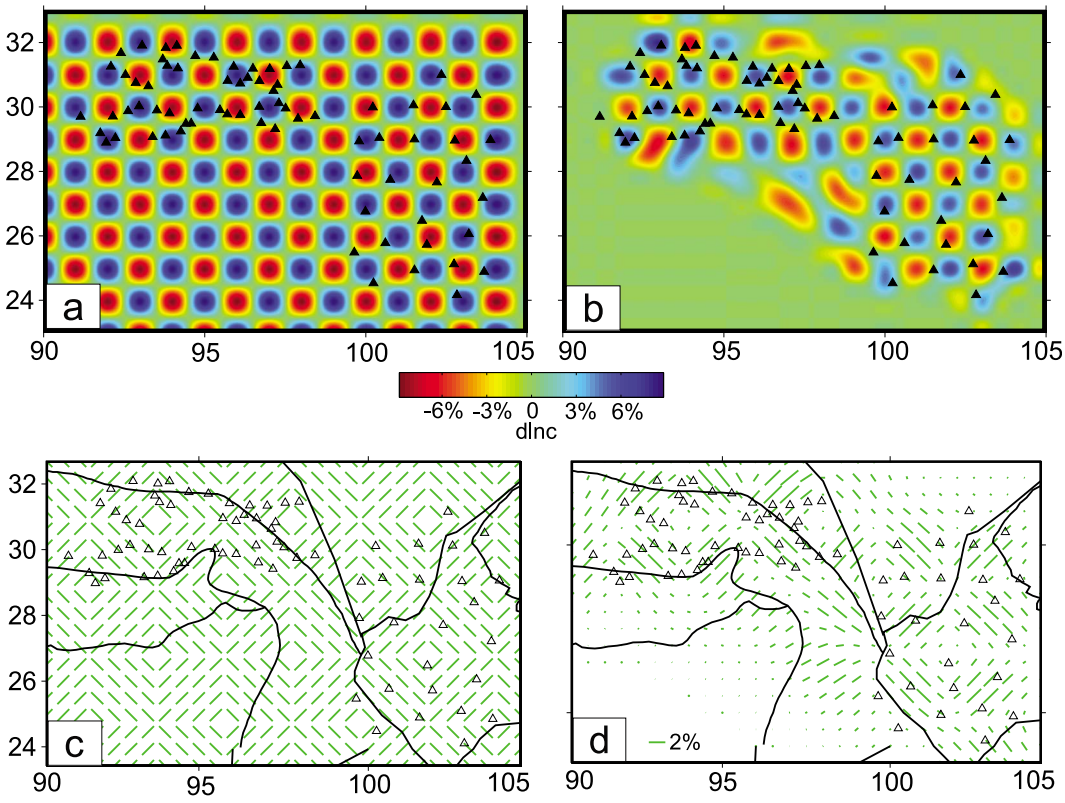

Figure 5. Checkerboard tests for the raypath coverage at $T = 30$ s: (a) 1° × 1° isotropic phase velocity checkerboard model; (b) recovery of isotropic phase velocity map; (c) 2° × 2° checkerboard model of azimuthal anisotropy; and (d) recovery of azimuthal anisotropy. The stations are shown as the triangles.

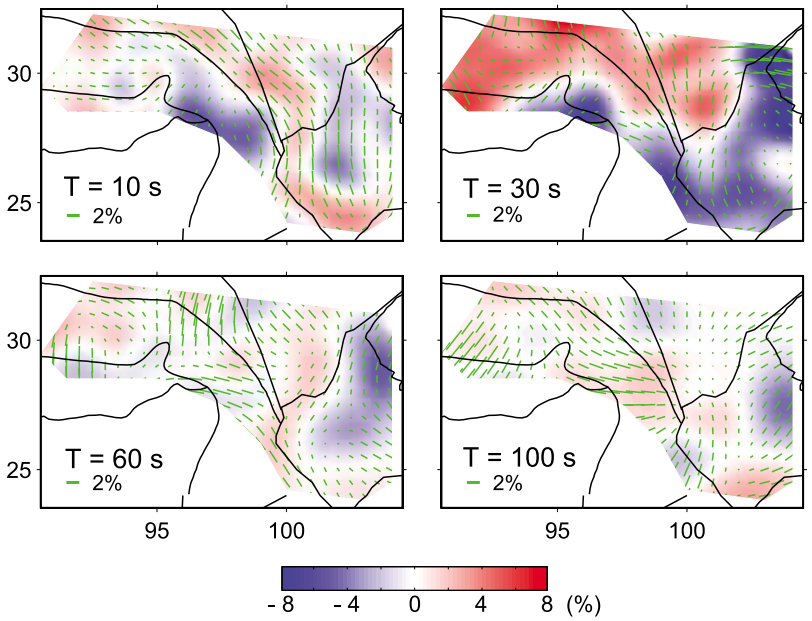

Figure 6. Variation of isotropic phase velocities and azimuthal anisotropy at $T = 10$, 30, 60, and 100 s. Color bar shows the value of phase velocity perturbation in percent with respect to the average value at the corresponding period in Figure 3b. The green bars show the magnitude (in percent) and fast polarization direction of azimuthal anisotropy.

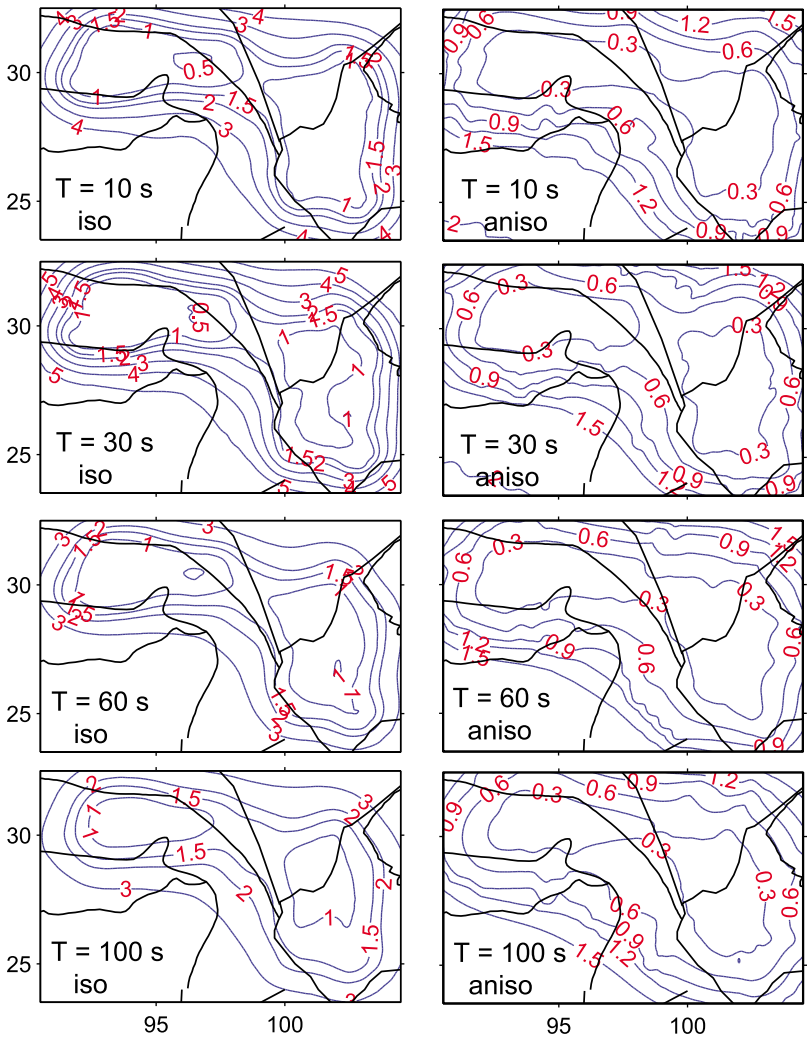

Figure 7. Posterior errors (in percent) of (left) isotropic phase velocities and posterior errors (in percent) of (right) the magnitude of azimuthal anisotropy at T = 10, 30, 60, and 100 s. The corresponding phase velocity and azimuthal anisotropy variations are shown in Figure 6.

here it may not yield accurate results. Therefore, we combine NA and linearized inversion in a stepwise approach: NA is used to obtain (point-wise) 1-D models of isotropic structure (with uncertainties), which are then used in linearized inversion for 3-D heterogeneity and anisotropy.

[23] In the first step, for each point on a regular grid we use NA to estimate a 1-D profile of isotropic Vs using the phase speed as a function of period (T = 10–150 s) inferred from the phase velocity maps. We constrain nine model parameters: Moho depth and Vs of three crustal layers (each with similar thickness) and five upper mantle layers (Moho–90 km, 90–130 km, 130–170 km, 170–220 km, 220–300 km). To account for the large variation in Moho depth (40–75 km), for each grid point we use a reference model with crustal thickness obtained from receiver functions [*Zurek et al.*, 2005; *Xu et al.*, 2007] or from the global reference model Crust 2.0 (http://igppweb.ucsd.edu/~gabi/crust2.html). The search range for Moho depth is ±5 km around this reference, and the reference for Vs as well as the permissible search range (for each layer) is taken from *Yao et al.* [2008].

[24] In the second step, we use the point-wise 1-D isotropic Vs model obtained from NA as the starting point for linearized inversion for Vs azimuthal anisotropy in the crust and upper mantle [*Montagner and Nataf*, 1986]. That is, at each grid point we use a different reference model. At location M, the Rayleigh wave (isotropic and azimuthally anisotropic) phase velocity perturbation δc_R (M, ω, ψ) is expressed as

$$\delta c_{\mathrm{R}}(M,\omega,\psi) = \int_0^H \left[\frac{\partial c_{\mathrm{R}}}{\partial A}(\delta A + B_{\mathrm{c}}\cos 2\psi + B_{\mathrm{s}}\sin 2\psi) + \frac{\partial c_{\mathrm{R}}}{\partial C}\delta C + \frac{\partial c_{\mathrm{R}}}{\partial F}(\delta F + H_{\mathrm{c}}\cos 2\psi + H_{\mathrm{s}}\sin 2\psi) + \frac{\partial c_{\mathrm{R}}}{\partial L}(\delta L + G_{\mathrm{c}}\cos 2\psi + G_{\mathrm{s}}\sin 2\psi)\right]\frac{\mathrm{d}z}{\Delta h}. \quad (2)$$

The parameters A, C, F, L, N describe the equivalent transverse isotropic medium with a vertical symmetry axis,

which implies averaging over all azimuths. The amplitudes of the cosine and sine terms (B_c, B_s, G_c, G_s, H_c, H_s) constrain the 2ψ azimuthal variation of A, L, and F. For each grid point, the kernels $\partial c_R/\partial p_i$ are calculated from the local 1-D profile (from NA) using normal mode theory [*Montagner and Nataf*, 1986]. In (2) the integration is from the surface ($z = 0$) to the maximum depth of the inversion ($z = H$), which we set to 280 km, and Δh is the normalization thickness for the calculation of sensitivity kernels. In this inversion, we consider the posterior error in phase velocity (section 3, Figure 7), and final errors in the model parameters are estimated from the posterior covariance matrix. We use a Gaussian correlation function with a correlation length that increases linearly from 20 km at the surface to 40 km at 280 km depth. Rayleigh phase velocities are mainly sensitive to L, that is, the derivatives with respect to A in the upper mantle, C, and F are small, so that mainly three parameters (L, G_c, G_s) can be resolved [*Montagner and Nataf*, 1986; *Simons et al.*, 2002] although all elastic parameters in (2) and density are simultaneously inverted for. Finally the azimuthally anisotropic velocity of vertically polarized shear wave is given by

$$\hat{\beta}_{SV} \approx \sqrt{\frac{L + G_c \cos 2\psi + G_s \sin 2\psi}{\rho}}, \tag{3}$$

where ρ is the density, and since G_c and G_s are usually much smaller than L we can write,

$$\hat{\beta}_{SV} \approx \beta_{SV}\left(1 + \frac{G_c}{2L}\cos 2\psi + \frac{G_s}{2L}\sin 2\psi\right), \tag{4}$$

where $\beta_{SV} = \sqrt{L/\rho}$ is the isotropic part of the vertically polarized shear wave speed. The strength of azimuthal anisotropy is $A_{SV} = \frac{1}{2L}\sqrt{(G_c)^2 + (G_s)^2}$ and the azimuth angle of fast polarization axis is $\phi = \frac{1}{2}\tan^{-1}(G_s / G_c)$.

[25] We note that, according to (2), the sensitive kernel for (G_c, G_s) is $\partial c_R/\partial L$. Indeed, the objective of the stepwise approach is to obtain with NA optimal estimates of the 1-D isotropic shear wave speeds (i.e., L) at each grid point, which allows (for each location) the calculation of sensitivity kernels $\partial c_R/\partial L$ for the subsequent inversion for the azimuthal anisotropy parameters G_c and G_s.

5. The 3-D Heterogeneity and Azimuthal Anisotropy

[26] Figure 8 shows the lateral variation of shear wave speed and azimuthal anisotropy in the crust and upper mantle (obtained from the 1-D profiles described above; see also the examples in Appendix B and Figure B1), and Figures 9 and 10 show, respectively, the wave speed and the wave speed perturbations (relative to the reference model) for a series of (vertical) crust-mantle sections across SE Tibet. Since for the azimuthal anisotropy inversion we use dispersion data up to 100 s, we only show the results for azimuthal anisotropy up to 150 km (Figure 8).

[27] For the MIT array area (Figure 1b) the inferred wave speed variations are generally consistent with our previous study [*Yao et al.*, 2008], but the structures are better resolved and the data used here constrains lithosphere structure in a larger region. The Lhasa Block, north of the Himalayan Thrust Belt, is marked by low wave speeds at middle crustal depth (Figures 9 and 10, profiles AA', BB', EE', and FF'). The Songpan-Ganze fold is also slow at middle/lower crustal depth, but with substantial lateral variation in intensity or depth/thickness of low velocity layer (Figures 9 and 10, profiles AA', BB', CC', DD', and HH'). The crust of the Yangtze Block is generally fast (Figure 8b), but low speeds appear near major fault zones, such as the Red River fault (Figure 8a), the middle crust of Xiaojiang fault zone (Figure 8b, profiles CC' and II' in Figures 9 and 10), and the middle and lower crust around Lijiang fault (Figure 8c, profiles CC' and DD' in Figures 9 and 10). At uppermost mantle depths (that is, 80 and 110 km, Figures 8d and 8e), the Qiangtang Block and the region around the Bangong-Nujiang suture appear fast. Near the margin of the study region, the upper mantle beneath the Lhasa Block is fast but further east wave speeds are average or slightly below average (Figures 8d and 8e). A conspicuous low-velocity zone is imaged in the uppermost mantle (80–150 km depth) around the western margin of the Yangtze Block and the Red River fault zone (Figure 8).

[28] The 3-D inversions reveal substantial variation of azimuthal anisotropy with depth (Figure 8). Azimuthal anisotropy is relatively weak (that is, A_{SV} is low) in the upper and middle crust (Figures 8a and 8b), but at 10 km depth the fast polarization axes (φ) reveal a prominent curvilinear pattern around the eastern Himalayan syntaxis (Figure 8a). This resembles the pattern of surface motion from GPS (Figure 11) but, as explained in the introduction, comparison between seismic anisotropy and GPS velocity fields is not straightforward (see also section 6.2, below). We also observe that the fast polarization axes at 10 km are nearly parallel to the major strike slip fault systems, i.e., Xianshuihe-Xiaojiang fault zone. At 25 km depth (Figure 8b) the fast direction is more complicated than that at 10 km: the fast direction in the Lhasa Block is nearly E-W oriented, while the Songpan-Ganze Fold Belt and Yangtze Block show a predominance of S-N fast direction.

[29] Figure 8 reveals dramatic changes in the pattern of azimuthal anisotropy from middle/lower crust (e.g., 50 km depth; Figure 8c) to the uppermost mantle (80 and 110 km depth; Figures 8d and 8e) in the Lhasa Block and beneath the Songpan-Ganze Fold Belt. Near the Indus-Tsangpo suture, around 93°E, the fast polarization changes from E-W at 50 km depth to N–S at 80 and 110 km depth (Figures 8d and 8e). At 50 km depth, the fast direction in the Songpan-Ganze Fold Belt and Yangtze Block is predominantly N–S (Figure 8c). However, in the uppermost mantle (80 and 110 km; Figure 8d and 8e) the fast axes generally follow the shape of the slow structure along the western margin of Yangtze Block. [We notice a coincidence with the orientations of the Lijiang-Muli and Red River faults, but since such local correlations may not be meaningful we prefer the statistical analysis described below.] The regions north and south of 26°N have nearly orthogonal fast propagation axes in the shallow mantle (Figures 8d and 8e). At 110 km depth (Figure 8e) the fast direction is approximately E-W near 26°N. Both in Yunnan and near the Bangong-Nujiang suture the fast direction at 150 km depth (Figure 8f) differs

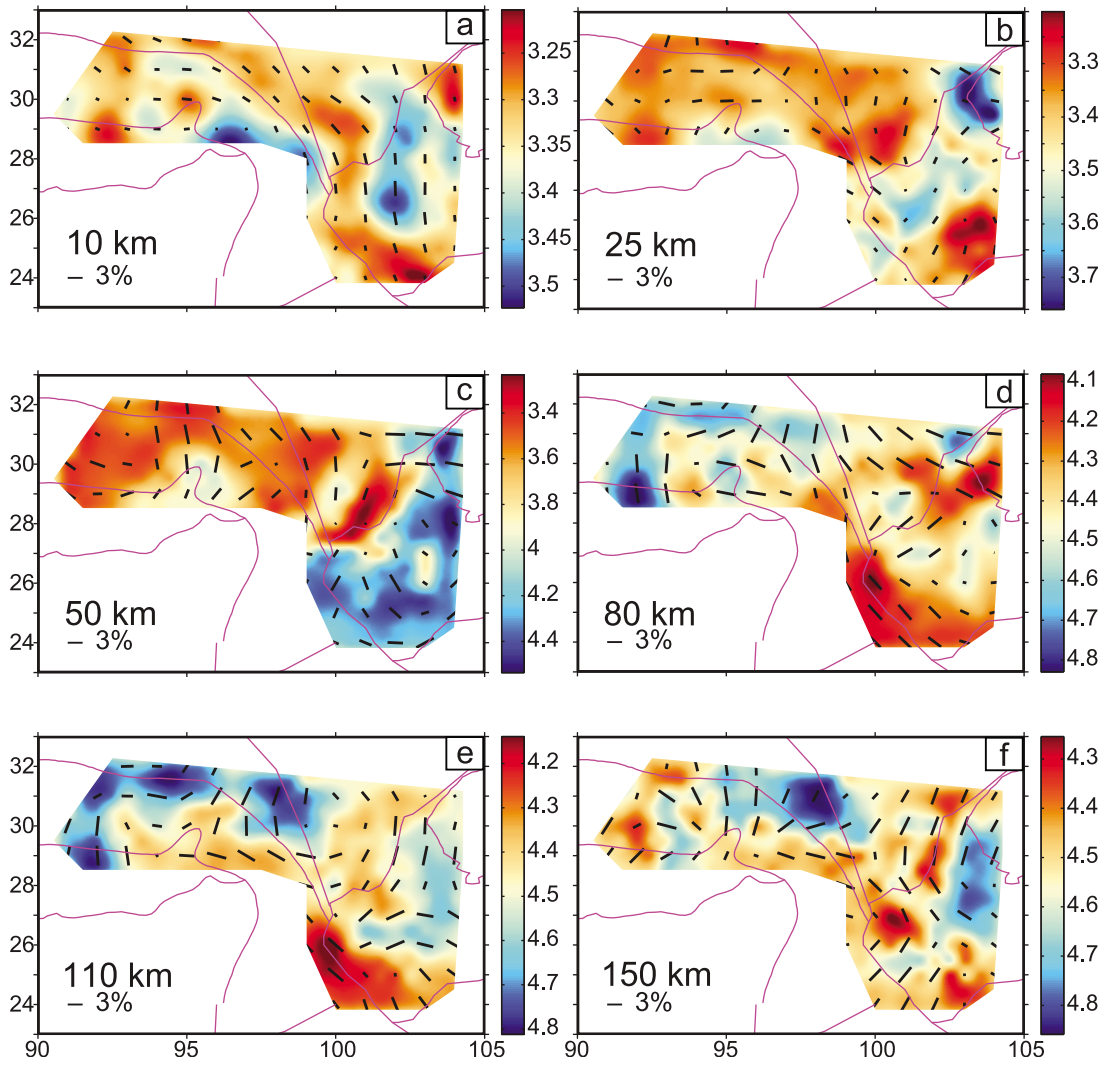

Figure 8. Variation of absolute shear wave speeds (color image) and azimuthal anisotropy (short black bars) in the crust and uppermost mantle beneath SE Tibet. The color bars show the color scale of shear wave speeds (km/s).

from that at 80 and 110 km. However, the resolution and reliability of anisotropy obtained at 150 km is not as good as shallower uppermost mantle depth due to the degraded azimuthal path coverage and depth resolution at longer periods. Hereinafter, we restrict the discussion to azimuthal anisotropy to a depth of 120 km.

6. Discussion

6.1. Crustal Low-Velocity Zones: Evidence of Crustal Flow?

[30] Our tomographic images reveal widespread low velocity zones (LVZs) (Figures 8–10) in the crust and locally in the lithospheric mantle beneath SE Tibet and SW China. Before discussing crustal LVZs in more detail, we emphasize that they are anomalous relative even to a crust that is, as a whole, seismically slower than the global average crust.

[31] The presence of midcrustal LVZs beneath the Lhasa Block in southern Tibet is consistent with the magnetotelluric results that exhibit high conductivity in the middle crust [*Unsworth et al.*, 2005; *Wei et al.*, 2001] and which suggest a weaker and partial molten middle crust. Numerical models [e.g., *Beaumont et al.*, 2004] with a low viscosity and partially molten middle crust explain how midcrustal rocks (e.g., the high-grade metamorphic rocks described by *Grujic et al.* [2002]) could have been exhumed to the surface [*Hodges et al.*, 2001; *King et al.*, 2007]. The (seismically) normal lower crust of southern Tibet, underlying the midcrustal LVZ observed here, may represent subducted Indian crust [*Percival et al.*, 1992]. Indeed, *Priestley et al.* [2008] explain the observed seismicity in the shallow and lower crust with a cool, brittle upper "Tibetan" crust and a cold brittle low "Indian" crust, separated by a ductile, aseismic middle crust.

[32] The southern part of the Songpan-Ganze Fold Belt shows prominent velocity anomalies in both middle and

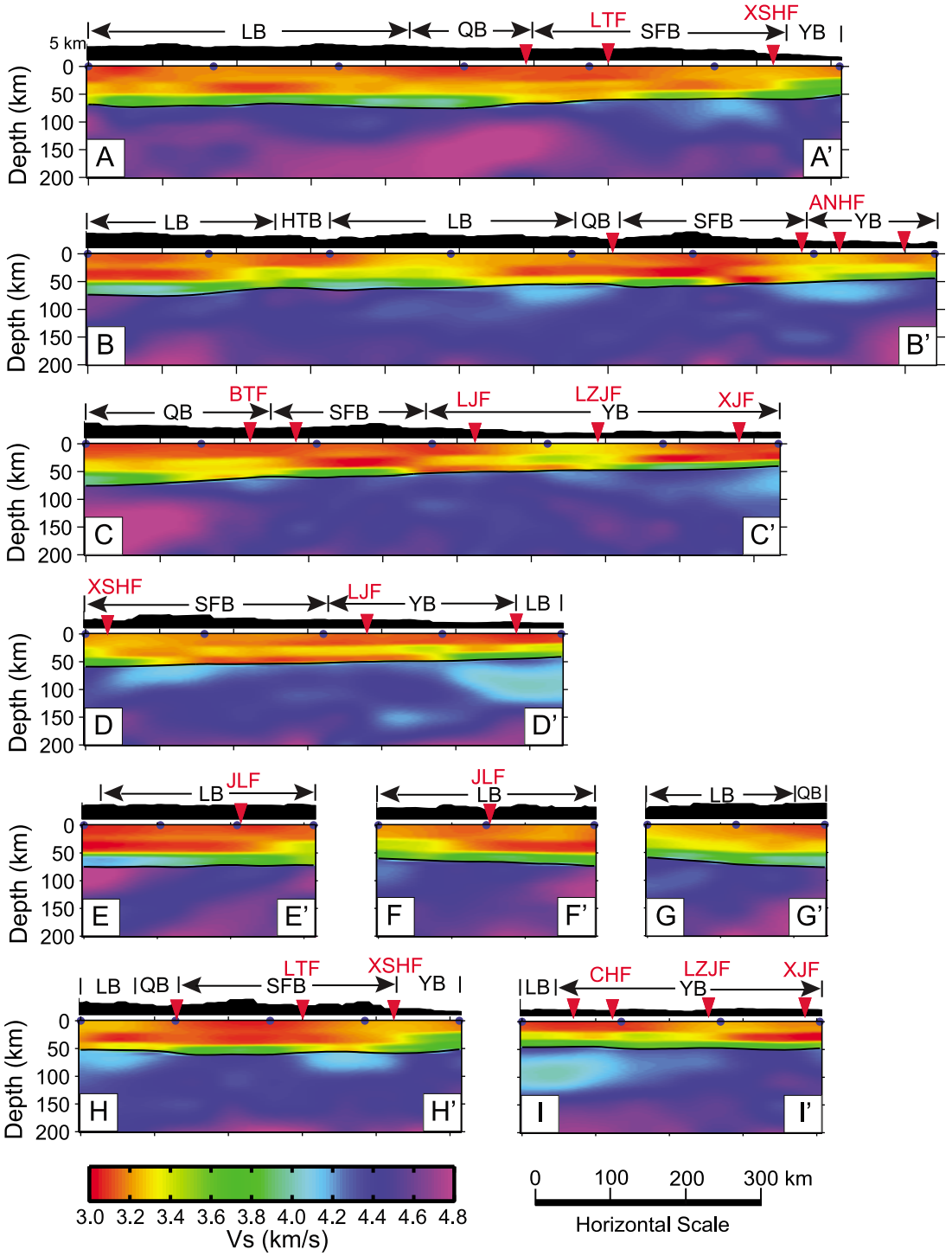

Figure 9. Absolute isotropic shear wave speeds across the nine profiles shown in Figure 1b (blue lines). Topography is depicted above each profile as the black area and the red triangles above it mark the location of major faults along each profile. The abbreviations for fault names (red) are the same as in Figure 1. The tectonic unit boundaries are shown as the black vertical lines on each topographic area. The abbreviations for the tectonic unit are as follows: LB, Lhasa Block; QB, Qiangtang Block; SFB, Songpan-Ganze Fold Belt; YB, Yangtze Block; HTB, Himalayan Thrust Belt. The thick black line (around 50–75 km depth) on each color profile indicates the Moho discontinuity. The wave speed (km/s) color scale and the horizontal length scale of profiles are shown as the color bar and scale ruler at the bottom, respectively.

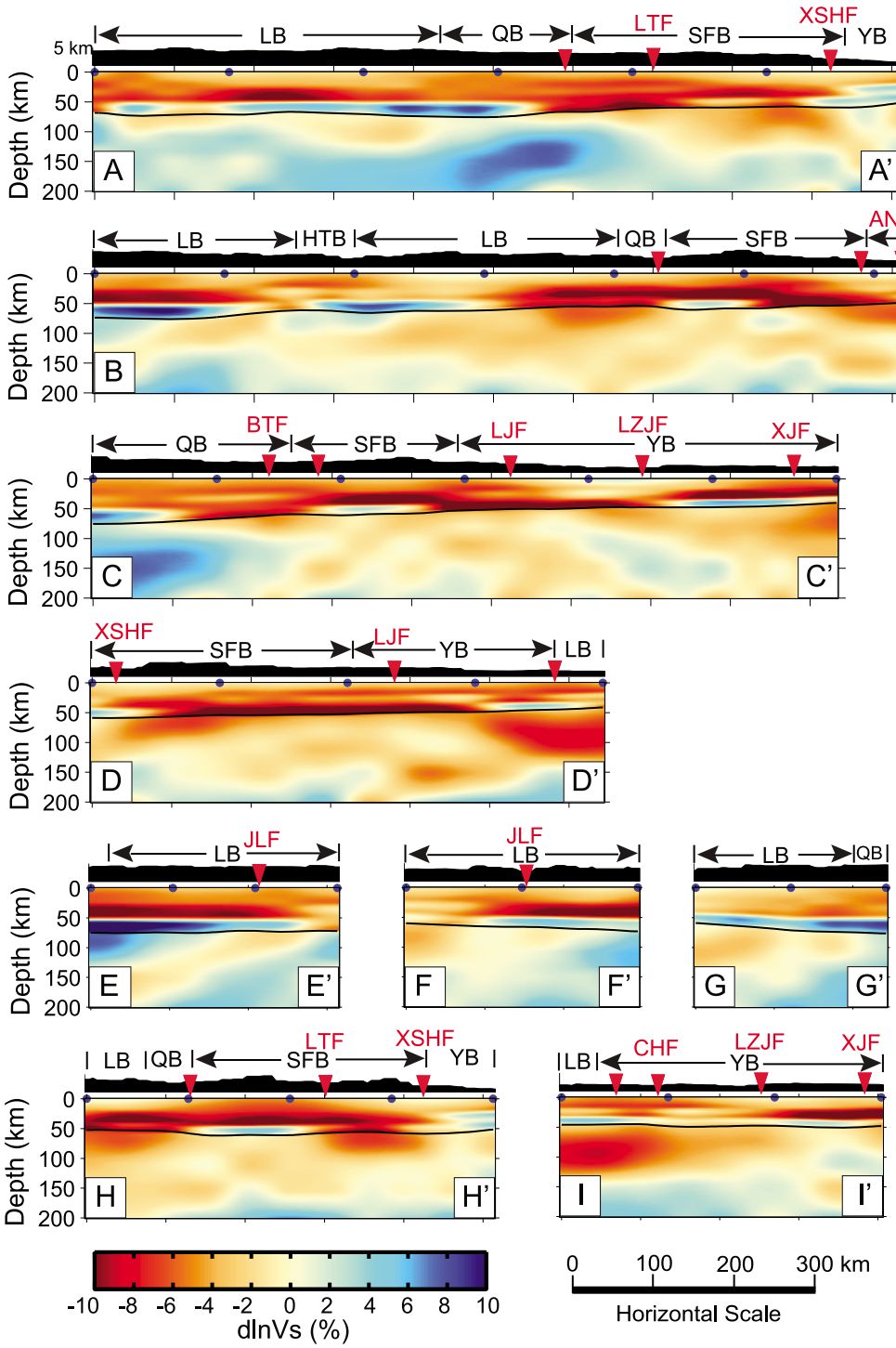

Figure 10. Same as in Figure 9 but for the perturbation of shear wave speeds (in percent) with respect to the reference model. The reference Vs in the crust linearly increases from 3.4 km/s at the surface to 3.85 km/s at Moho depth, which is (approximately) inferred from the global Crust 2.0 model (http://igppweb.ucsd.edu/~gabi/crust2.html) by averaging Vs separately of the upper, middle, and lower crust for all locations with crustal thickness larger than 40 km. The reference Vs in the upper mantle is from the global *ak135* model [*Kennett et al.*, 1995].

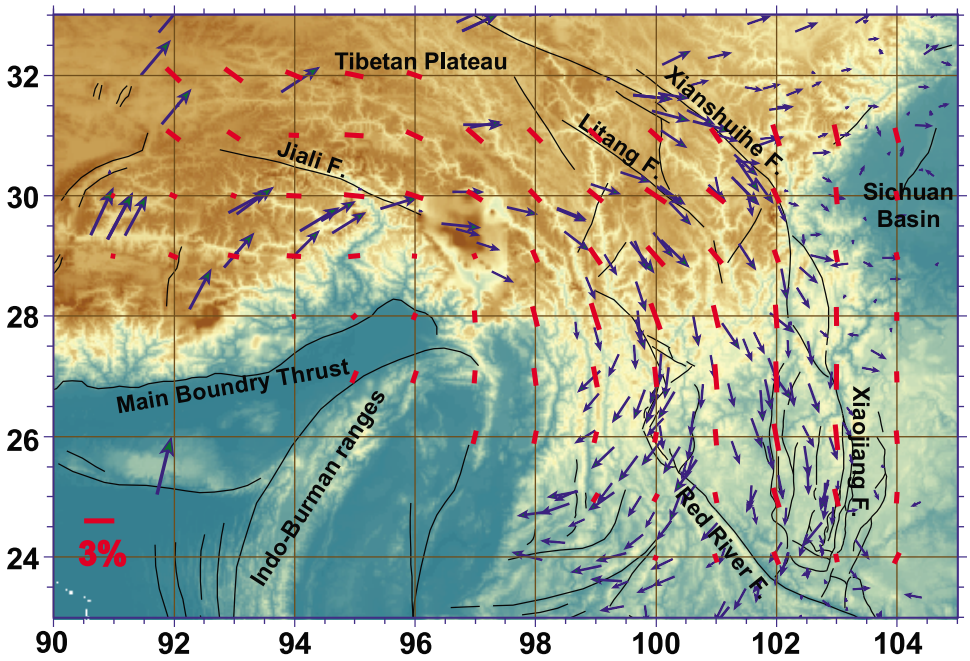

Figure 11. Observed azimuthal anisotropy at 10 km (red bars), local fault systems (black lines), and GPS velocity field (blue arrows) with respect to the South China Block. The sources of GPS measurements are from *Chen et al.* [2000], *Zhang et al.* [2004], and *Sol et al.* [2007].

lower crust, and LVZs are also present beneath the western Yangtze Block. As we observed before [*Yao et al.*, 2008], in some but not all areas, the (lateral) boundaries of the LVZs seem to coincide roughly with major faults in this area, e.g., Xianshuihe fault, Anninghe fault, and Luzhijiang fault (e.g., profiles AA', BB', CC', HH', and II' in Figures 9–10). However, the spatial resolution is not sufficient to draw more definitive conclusions about this potentially important structural relationship.

[33] It is likely that LVZs represent zones of ductile deformation, but by itself their presence neither confirms nor refutes the regional importance of crustal channel flow as suggested by *Royden et al.* [1997] and *Clark and Royden* [2000]. On the one hand, low shear wave speed implies low (elastic) rigidity and the spatial correlation of LVZs, zones of high (electric) conductivity [*Unsworth et al.*, 2005; *Bai et al.*, 2010; *Rippe and Unsworth*, 2010], high crustal Poisson's ration [*Hu et al.*, 2005; *Xu et al.*, 2007], and areas of steep geothermal gradients [*Hu et al.*, 2000] are all consistent with the presence of partial melt in the deep crust. Our tomographic images thus suggest the ubiquitous presence of weak zones in the crust below SE Tibet and SW China. On the other hand, it is not yet known if these zones are sufficiently interconnected to enable regional scale channel flow. Our tomographic images suggest substantial lateral heterogeneity, and since we do not know what level of wave speed reduction implies a sufficient reduction in strength to allow flow, we do not know if ductile deformation is confined to isolated LVZs or if flow in other (slow) parts of the crust or lithospheric mantle help create regional scale conduits.

[34] If regional scale flow occurs its pattern will be more complicated than predicted from models with depth dependent viscosity. In particular, LVZs may be truncated by major faults at depth. This observation suggests that major faults influence (or be themselves influenced by) the pattern of flow and, hence, the style of regional deformation.

6.2. Crust and Mantle Deformation: Coupled or Decoupled?

[35] Crustal channel flow [e.g., *Royden et al.*, 1997] implies that the weak layer decouples deformation in the shallow crust from that in the lithospheric mantle. In contrast, geodynamical modeling (constrained by GPS observations, quaternary fault slip data, and shear wave splitting measurements) generally favor vertically coherent deformation in the lithosphere [e.g., *Flesch et al.*, 2005]. Resolving this controversy is key to understanding lithospheric deformation of (eastern) Tibet, but several issues must be considered.

[36] First, the level of crust-mantle coupling does not need to be the same everywhere. *Flesch et al.* [2005] and *Sol et al.* [2007] suggest decoupling in Yunnan province and vertically coherent deformation further north, and *Bendick and Flesch* [2007] suggest that crustal flow and lithospheric coupling can coexist in northern Tibet if the viscosity contrast between crust and upper mantle is much smaller than implied in canonical crustal models [e.g., *Royden et al.*, 1997; *Clark and Royden*, 2000]. The results of our tomographic studies suggest that the level of coupling may well vary on smaller scales and that it may be scale dependent. The localized nature of LVZs (see above) suggests strong lateral variation in crustal rheology, which may mean that also the level of crust-mantle coupling varies laterally. Effective decoupling may occur across large (or interconnected smaller) LVZs, whereas deformation may appear vertically coherent elsewhere, even if (small) LVZs are present.

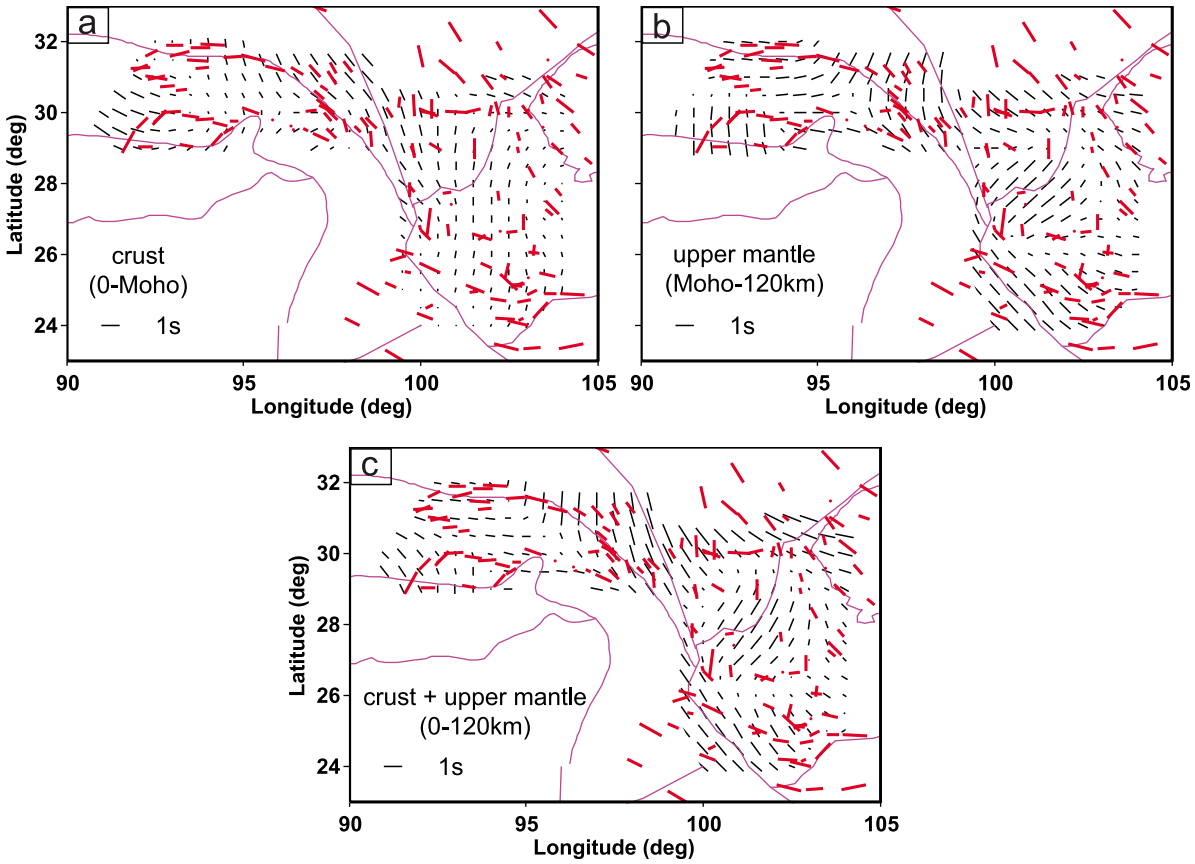

Figure 12. Comparison of the observed shear wave splitting measurements (red thick bars, from *Lev et al.* [2006], *Sol et al.* [2007], and *Wang et al.* [2008]) with the predicted shear wave splitting time and fast direction (black bars) in (a) the crust (from surface to Moho depth), (b) upper mantle (from Moho to 120 km depth), and (c) crust and upper mantle (from surface to 120 km depth) using the obtained 3-D azimuthally anisotropic model in this study (Figure 8).

[37] Second, conclusions about crust-mantle coupling based on comparison between GPS data and seismic anisotropy (for instance from shear wave splitting) involve many assumptions. In contrast to anisotropy, GPS velocities depend on the geographical reference frame, and the vectors would change if a different reference is used. This can be remedied by taking the spatial derivative (to obtain the frame-invariant strain rate). Furthermore, seismic anisotropy relates to structures (or fabric) formed over long periods of geological time, often during complex strain histories, whereas the gradient of GPS velocities yields the present-day (instantaneous) strain rate. Direct comparison between the two is meaningful only if a simple deformation history can be assumed.

[38] Third, GPS observations relate to the near-surface whereas shear wave splitting reflects the accumulative effect of anisotropy over a large (and unknown) depth range. To constrain the style of deformation in the lithosphere one often assumes that splitting observed at the surface has an upper mantle origin [*Flesch et al.*, 2005; *Sol et al.*, 2007; *Wang et al.*, 2008]. But with a thick and highly deformed crust this may not be justified. For typical crustal rocks, shear wave split times are about 0.1–0.2 s per 10 km; mica and amphibole lattice preferred orientations play a major role for crustal anisotropy [*Barruol and Mainprice*, 1993; *Weiss et al.*, 1999], similar as the role of olivine for upper mantle anisotropy. For the thick Tibetan crust (70–80 km) shear wave splitting from crustal anisotropy can be on the order of 1 s, which is similar to the observed splitting in SE Tibet [*Lev et al.*, 2006; *Wang et al.*, 2008]. To get better insight into crust-mantle coupling we need to determine the relative contributions of crust and mantle to the observed splitting.

6.2.1. Differences Between Crust and Mantle Anisotropy

[39] In order to quantify the relative contributions from crust and mantle anisotropy to the observed shear wave splitting we compare the observations with predictions from our 3-D anisotropy model from surface wave array tomography. We can predict observed split times and polarization axes if we assume a horizontal symmetry axis and vertically incident shear waves [*Montagner et al.*, 2000; *Simons et al.*, 2002]. We first calculate the split time and polarization for the crust (Figure 12a). The predicated split time is ~1 s in the plateau area, where the crust is 70–80 km thick (Figure 1b), and much smaller off-plateau in Yunnan. The observed split time is also ~1 s [*Lev et al.*, 2006; *Wang*

et al., 2008], which suggests that the contribution from plateau crust cannot be ignored.

[40] The estimated split times and directions from the mantle part of our model (that is, Moho–120 km depth), displayed in Figure 12b, are substantially different from the splitting inferred from 3-D crustal anisotropy (Figure 12a). The most obvious feature is the larger split time in Yunnan (which for this depth range is ~1 s). The polarization predicted from the upper mantle is mostly NW–SE in the southern part of the study region, while north of 26°N the direction is mostly NE–SW. The implied change in upper mantle deformation across ~26°N is consistent with observations from shear wave splitting [*Lev et al.*, 2006] and has been attributed to a transition of tectonic boundary conditions [*Sol et al.*, 2007]. In southern Tibet, west of 93.5°E, the fast polarization direction estimated from azimuthal anisotropy in the crust (Figure 12a) is quite different from that estimated from anisotropy only in the uppermost mantle (Figure 12b) around the Bangong-Nujiang suture and Indus-Tsangpo suture, implying a different deformation pattern in the crust and upper mantle around these suture zones.

[41] Splitting calculated from crust and upper mantle combined (Figure 12c) is more similar to that from the upper mantle (Figure 12b) than from the crust (Figure 12a), reflecting, in general, a larger contribution by upper mantle anisotropy, especially in the Yangtze block where crustal thickness is not large. In some regions the fast directions from crust (Figure 12a) and upper mantle (Figure 12b) are similar, for instance, around Sichuan basin and part of the Songpan-Ganze Fold Belt. This alignment enhances the (total) split times. In some other areas, for instance in the Lhasa Block, crust and upper mantle splitting have nearly orthogonal fast directions, which can explain the smaller split times.

[42] In Figure 13 we compare predictions from our 3-D model with observed fast polarizations. For this purpose, we only consider observations with significant splitting ($\delta t >$ 0.2 s), and in order to compare the fields at comparable spatial resolution we smooth the observed data to suppress variations on scales that cannot be resolved tomographically (see Appendix C). Differences between observed and predicted polarization directions are large for splitting calculated from crustal anisotropy (Figure 13a). For mantle anisotropy the differences are smaller (Figures 13b and 13e), but in over 20% of the study region the angle differences exceed 60°. If splitting is calculated from anisotropy in crust and mantle combined, the angle difference is less than 30° in about 55% of the cases (Figure 13c and 13f).

[43] This discrepancy between the predicted and observed splitting fast directions can have several causes. First, mantle anisotropy at depths larger than the base of the tomographic model (at z = 120 km), such as anisotropy due to subduction beneath the Himalaya and Burma ranges, is not included in the predictions. Second, observed splitting directions may have large uncertainty caused by noise and uneven azimuthal data coverage. Third, the directions inferred from surface wave array tomography have uncertainties due to uneven azimuthal coverage and regularization of the inversion (see sections 3 and 4, above). Finally, the calculation of the splitting parameters assumes vertical incidence and a horizontal orientation of the fast axis [*Simons et al.*, 2002], but the data used have a nonzero incidence angle and dipping axes of symmetry cannot be excluded.

[44] The above observations suggest important differences in crust and mantle anisotropy beneath SE Tibet. The analysis confirms that, overall, upper mantle anisotropy contributes more to observed splitting than the crust. In fact, the contribution from crustal anisotropy is negligible in Yunnan. For stations on the high plateau of SE Tibet, however, the contribution from the crust (up to ~1 s split time) is comparable to that from the mantle (Figure 12). Combined, the observed splitting and the 3-D model of azimuthal anisotropy suggest substantial depth variations of anisotropy. This cannot be resolved with traditional shear wave splitting analysis [e.g., *Lev et al.*, 2006], but it may become possible to constrain depth variations with finite frequency shear wave splitting tomography [*Chevrot*, 2006; *Long et al.*, 2008; *Sieminski et al.*, 2008].

6.2.2. Implications for Understanding Crust-Mantle (De)Coupling

[45] The conclusion by *Flesch et al.* [2005] and *Wang et al.* [2008] that crust and mantle deform coherently follows, in part, from the assumption that the observed splitting at the surface originates in the upper mantle. However, the above analysis shows that on the plateau proper, that is, in some regions west of Sichuan basin, the contribution to splitting from the thick crust is comparable to that from the upper mantle. Over large areas there appear significant differences in the pattern of crust and upper mantle azimuthal anisotropy (Figures 8 and B1). Indeed, the difference between fast polarization axes calculated from anisotropy in the crust (0–Moho) or mantle (Moho–120 km) exceeds 45° in about 75% of the study area (Figure 14). This is consistent with *Yi et al.* [2010] who found that in eastern Tibet the pattern of Rayleigh Wave azimuthal anisotropy at intermediate periods (T = 30 s) differs from that at long periods (T = 100 s).

[46] The variation of azimuthal anisotropy with depth (Figures 8, 14, and B1) suggests that in SE Tibet parts of the crust and upper mantle deform (or have deformed) differently from one another. The data do not resolve a correlation between the presence of LVZs and the strength of azimuthal anisotropy, but in many regions (e.g., in Songpan-Ganze Fold Belt) the lower crust has stronger azimuthal anisotropy (~3%–4%) than the upper and middle crust (~2%). Moreover, Love-Rayleigh wave analysis [*Huang et al.*, 2010] suggests that LVZs coincide with regions where horizontally polarized shear waves propagate faster than vertically polarized waves ($V_{SH} > V_{SV}$). This might be indicative of more efficient flow in parts of the deep crust where temperatures are high or where differences in composition (e.g., volatile content, melt) localize ductile deformation.

[47] These observations appear incompatible with vertically coherent deformation of the crust-mantle system, but without knowing the actual processes that produce the azimuthal anisotropy it is not possible to make more conclusive statements. Anisotropy in the crust and lithospheric mantle can be caused or influenced by several factors, including the style of deformation (e.g., pure or simple shear [*Wang et al.*, 2008]), the presence or absence of cracks [*Crampin and Chastin*, 2003], crystal orientation (e.g., shape or lattice preferred orientation [*Savage*, 1999]), deformation fabric (e.g., S-C fabrics for shear deformation of mica [*Lloyd et al.*, 2009]), and in situ conditions such as temperature, stress,

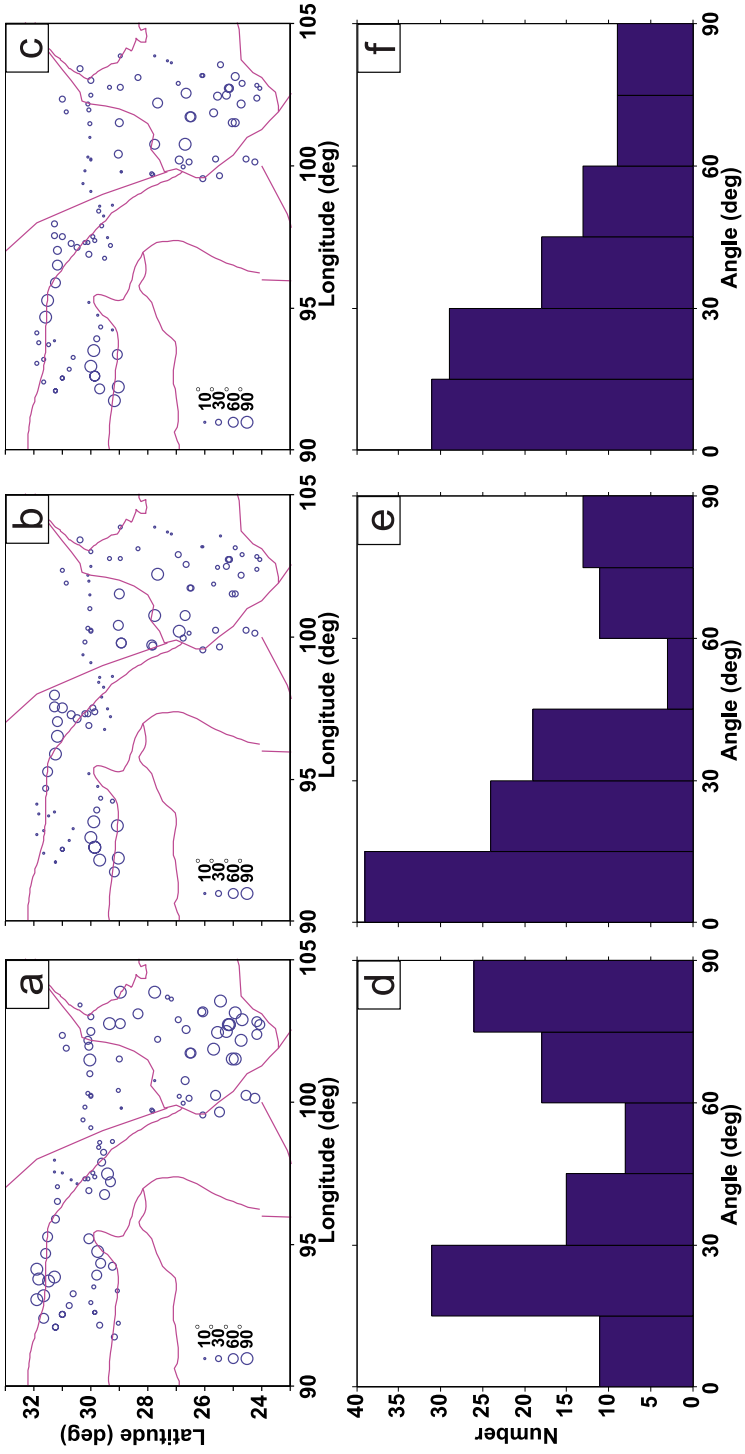

Figure 13. The spatial distribution of the angular difference (in degree, shown as the open circles) between the observed fast polarization axis and the polarization predicted from different depth ranges of our 3-D tomographic model: (a) crust (see Figure 12a), (b) upper mantle (see Figure 12b), (c) crust and upper mantle (see Figure 12c). For this comparison observations with split times larger than 0.2 s are spatially smoothed (black bars in Figure C1) to remove short wavelength variations that cannot be resolved tomographically. The associated histograms of the angular differences are shown in Figures 13d, 13e, and 13f, respectively, with the vertical axis the number of observations for comparison and the horizontal axis the angle difference (in degree).

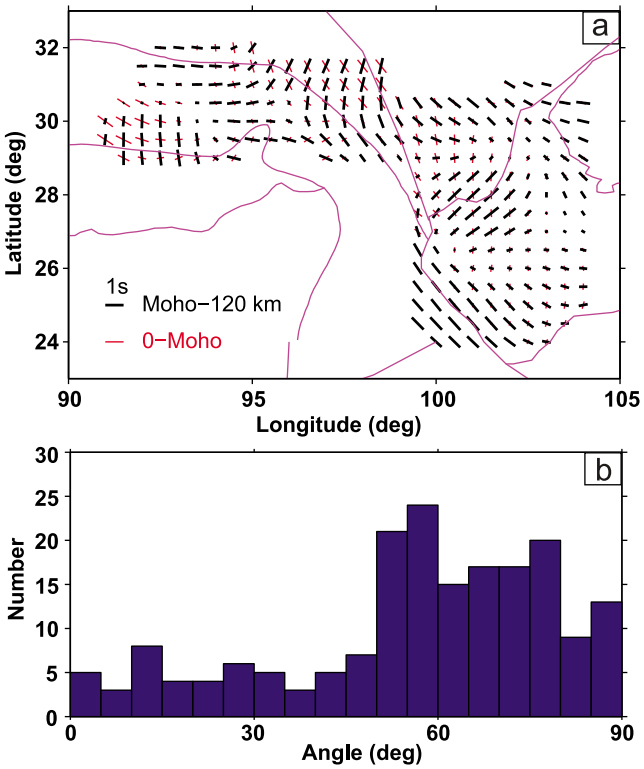

Figure 14. Comparison of the predicted shear wave splitting in the crust (red bars in Figure 14a) with that in the uppermost mantle (Moho–120 km) (black thick bars in Figure 14a). The histogram of the angle differences between red and black bars in Figure 14a, both with splitting time larger than 0.2 s is shown as Figure 14b, with the vertical axis the number of grid points in the study region for comparison and the horizontal axis the angle difference (in degree).

water content, and melt [*Karato et al.*, 2008]. Much like the lateral variations in elastic structure inferred here, these factors vary, and local differences between crust and mantle anisotropy may occur regardless of the level of mechanical coupling between crust and mantle. Most of our observations pertain to a regional scale, however.

7. Conclusions

[48] High-resolution surface wave tomography from ambient noise interferometry and teleseismic surface wave analysis provides important constraints on the structure and deformation of the lithosphere of SE Tibet and SW China. The main conclusions are as follows:

[49] 1. The lateral resolution of our surface wave array tomography in SE Tibet is ~100 km for the isotropic part of the model and ~200 km for azimuthal anisotropy.

[50] 2. Shear wave speed is relatively low in the entire crust, but locally the wave speed in the deep crust is anomalously low even compared to the average crust. Shear speed is also low in the lithospheric mantle beneath some crustal low velocity zones (LVZs).

[51] 3. LVZs occur near areas of low electrical resistivity [*Bai et al.*, 2010], high heat flow [*Hu et al.*, 2000], and high Poisson's ratios [*Xu et al.*, 2007]. It may be possible to attribute the low-wave speeds to anomalous composition or petrology, but the preponderance of evidence suggests that LVZs are mechanically weak probably due to the presence of partial (aqueous) melt.

[52] 4. Around the eastern Himalayan syntaxis, the LVZs form a largely interconnected but complex network with substantial lateral variation in depth, thickness, and strength of the anomalies. Some may be truncated by major faults (e.g., the Xianshuihe fault).

[53] 5. The surface wave data resolves changes of azimuthal anisotropy with depth, and the pattern of fast directions in the crust differs significantly from that in the mantle.

[54] 6. In general the upper mantle contribution to the observed splitting appears larger than the crustal contribution and off the plateau proper (in Yunnan, south of 26°N) upper mantle (azimuthal) anisotropy explains most of the observed shear wave splitting. However, on the high plateau west of Sichuan basin, splitting from the crust can be as large as that from the upper mantle. In regions (like the Tibetan plateau region) with a thick and structurally complex crust, it may thus not be justified to attribute splitting only to mantle anisotropy.

[55] 7. The radial change in anisotropy suggests that beneath much of SE Tibet the upper crust and lithospheric mantle deform (or have deformed) differently. If LVZs represent crustal scale "décollement zones," then the level of decoupling is likely to vary laterally along with changes in depth and strength of the LVZs.

[56] 8. The presence of mechanical weak zones and the depth variation of seismic anisotropy are qualitatively consistent with expectations from crustal flow models, but strong lateral heterogeneity suggests that the 3-D pattern of any such flow is complicated.

[57] 9. Our research suggests that regional scale deformation in SE Tibet occurs through the interplay between lithospheric units with or without crustal weak zones (that is, blocks with or without vertically coherent deformation) separated from one another by major faults. Understanding how such a system responds to regional tectonic stress may provide important keys to understanding the seismotectonics of this region and is therefore an important target for our future research.

Appendix A: Correction of Phase Velocity Measurements From the TS Analysis

[58] According to ray theory, used in traditional surface wave tomography, phase velocity or travel time is only sensitive to the structure along the great circle raypath. The average phase velocity at frequency ω between two stations at $A(\mathbf{r}_A)$ and $B(\mathbf{r}_B)$ in a perturbed earth mode can be expressed as

$$\overline{c}_{AB}^{RT} = \Delta_{AB} / t_{AB}^{RT}(\omega) = \Delta_{AB} \Big/ \int_A^B \frac{\mathrm{d}l}{c(\omega, \mathbf{r})}, \qquad \text{(A1)}$$

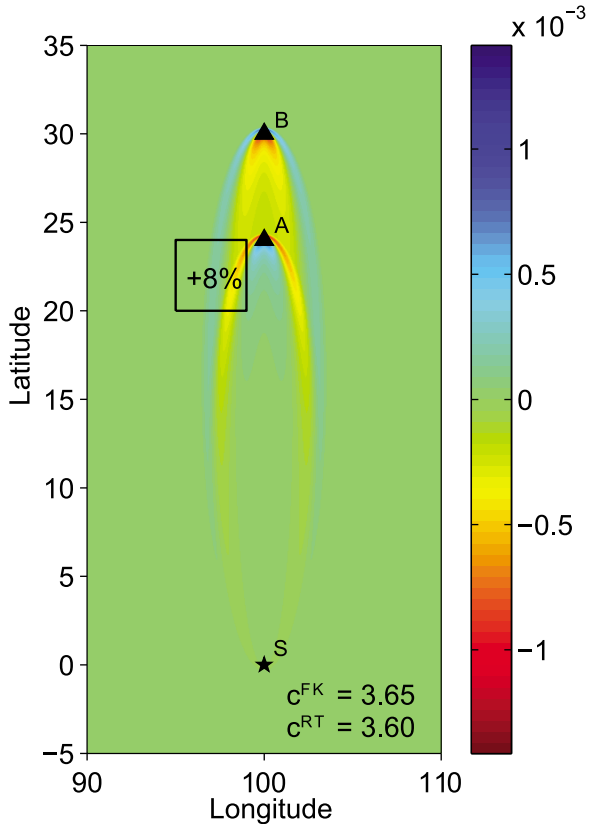

Figure A1. Surface wave finite sensitivity differential kernel K_ϕ^c (ω, $\mathbf{r}$; $\mathbf{r}_s$)$_{AB}$ (equation (A3)) at 30 s for two-station phase velocity analysis. The source is at S (star) and the two stations are at A and B (triangles). The background phase velocity is 3.6 km/s with anomaly (+8%) in the box near A. The calculation of the kernel is based on the method by *Zhou et al.* [2004] without considering the effect of source mechanism. The phase velocity between A and B based on ray theory (c^{RT}) is 3.6 km/s. The interstation phase velocity based on finite frequency theory (c^{FK}), e.g., from two-station cross-correlation analysis, is 3.65 km/s, which is about 1.5% larger than the ray based measurement, due to the effect of fast structure in the box but not on the interstation raypath between A and B.

where $c(\omega, \mathbf{r}) = c_0\ (\omega) + \delta c(\omega, \mathbf{r})$ gives the 2-D phase velocity distribution with c_0 as the reference phase velocity and $\delta c(\omega, \mathbf{r})$ as the 2-D phase velocity perturbation, Δ_{AB} is the great circle distance between A and B, and the integration is taken along the great circle path between A and B.

[59] Considering the finite frequency effect of surface wave propagation, we can express the phase travel time between $S(\mathbf{r}_S)$ and A as

$$t_{SA}^{FK}(\omega) = t_{SA}(\omega) + \frac{1}{\omega}\iint_{\Omega} K_\phi^c(\omega, \mathbf{r}; \mathbf{r}_S, \mathbf{r}_A)(\delta c/c_0)\mathrm{d}\Omega, \qquad \text{(A2)}$$

where $t_{SA}\ (\omega)$ is the reference travel time between S and A, $K_\phi^c\ (\omega, \mathbf{r}; \mathbf{r}_s, \mathbf{r}_A)$ is the 2-D phase sensitivity kernel to phase velocity, and the integration is computed at the spherical surface Ω of the Earth. Δ_{SA} (or Δ_{SB}) is the great circle distance between S and A (or B). Therefore, the finite frequency travel time of surface waves based on cross-correlation method between the two stations at A and B is given by

$$t_{AB}^{FK}(\omega) = t_{SB}^{FK} - t_{SA}^{FK} = (t_{SB} - t_{SA}) + \frac{1}{\omega}\iint_{\Omega} K_\phi^c(\omega, \mathbf{r}; \mathbf{r}_S)_{AB}(\delta c/c_0)\mathrm{d}\Omega, \qquad \text{(A3)}$$

where $t_{SB} - t_{SA} = (\Delta_{SB} - \Delta_{SA})/c_0$ is the differential reference travel time between A and B, and $K_\phi^c\ (\omega, \mathbf{r}; \mathbf{r}_s)_{AB} = K_\phi^c\ (\omega, \mathbf{r}; \mathbf{r}_s, \mathbf{r}_B) - K_\phi^c\ (\omega, \mathbf{r}; \mathbf{r}_s, \mathbf{r}_A)$ is the 2-D differential phase sensitivity kernel for two-station analysis. Figure A1 shows one example of the windowed differential kernel at $T = 30$ s with a reference phase velocity 3.6 km/s using the phase kernel expression in the work of *Zhou et al.* [2004] without considering effect of source mechanism. The average interstation phase velocity in the TS method based on finite frequency theory can be approximated as

$$\bar{c}_{AB}^{FK} = (\Delta_{SB} - \Delta_{SA})/t_{AB}^{FK}(\omega), \qquad \text{(A4)}$$

provided that the source is almost along the great circle path linking the two stations [see *Yao et al.*, 2006].

[60] In a generic heterogeneous medium, $\bar{c}_{AB}^{FK}$ may be different from $\bar{c}_{AB}^{RT}$. However, our approach to invert for both isotropic and azimuthally anisotropic phase velocity maps (section 3) is based on ray theory. In order to suppress contributions from structure outside the interstation raypath on the tomographic inversion results, we perform the following scheme to calculate an approximately ray theory-based interstation phase velocity measurements from the observed finite frequency measurements. First, we use the global crust and upper mantle model from *Shapiro and Ritzwoller* [2002] to calculate the phase velocity map $c(\omega, \mathbf{r})$ at each frequency ω (Figure A2b) and consequently the reference (average) phase velocity c_0 and the phase velocity perturbation $\delta c(\omega, \mathbf{r})$ in SE Tibet and surrounding area. From the model, we then calculate the difference of phase velocities between finite frequency approach and ray theory approach as

$$\delta\bar{c}_{AB}(\omega) = \bar{c}_{AB}^{FK}(\omega) - \bar{c}_{AB}^{RT}(\omega). \qquad \text{(A5)}$$

If the observed average interstation phase velocity from the TS approach [*Yao et al.*, 2006] is $\bar{c}_{AB}^{TS}(\omega)$, the corrected interstation phase velocity after suppressing the finite frequency effect is given by

$$\tilde{c}_{AB}^{TS}(\omega) = \bar{c}_{AB}^{TS}(\omega) - \delta\bar{c}_{AB}(\omega). \qquad \text{(A6)}$$

We repeat this process for every station pair for each earthquake at every period for our TS measurements and

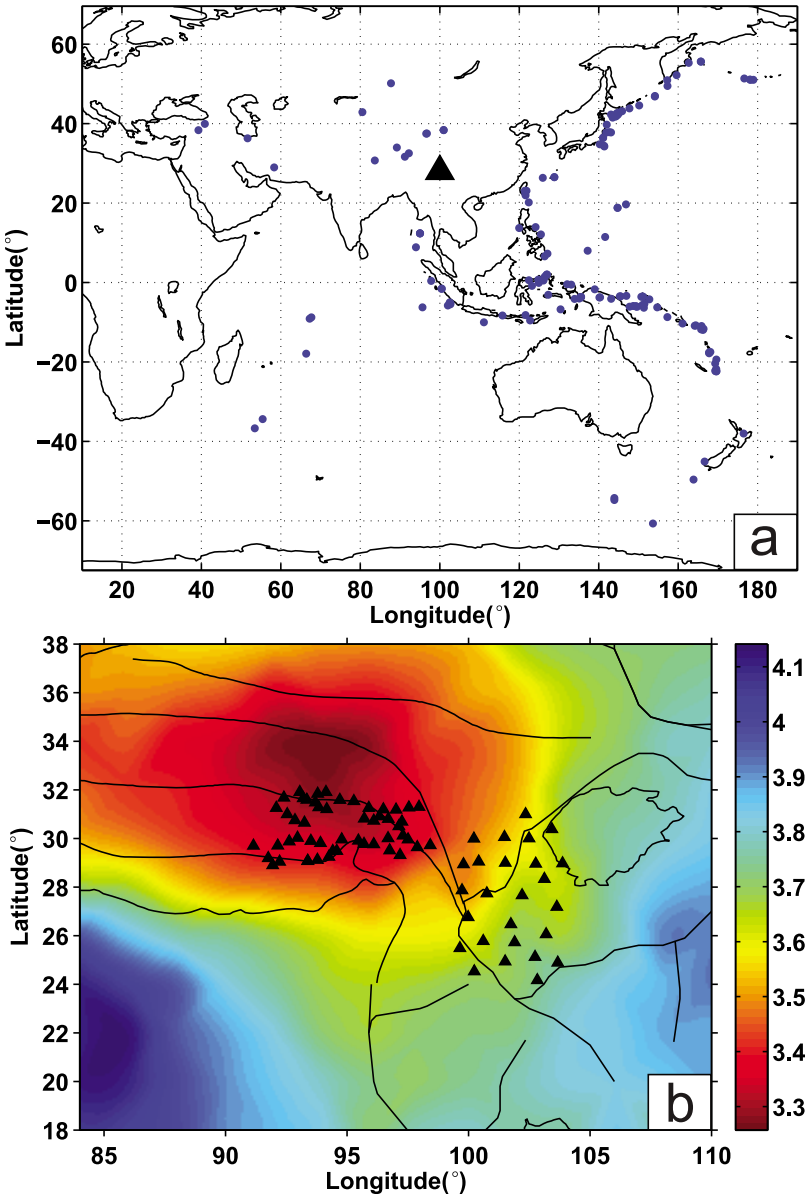

Figure A2. (a) Teleseismic events (blue dots) used for TS analysis. (b) Rayleigh wave phase velocity maps at 30 s in SE Tibet and adjacent regions from the global crust and upper mantle model [*Shapiro and Ritzwoller*, 2002]. In Figures A2a and A2b, the black triangles shows the location of array stations used in this study.

finally obtain the corrected interstation phase velocity measurements $\tilde{c}_{AB}^{TS}(\omega)$ within the period band 20–150 s for 16,386 interstation paths from about 150 earthquakes (Figure A2a). For each station pair, we average the dispersion curves from different events and finally obtain 2232 interstation average dispersion curves. The average phase velocity dispersion curve in the study area is thus calculated by taking the mean of all the interstation average dispersion curves. As shown in Figure A3, the original average phase velocity dispersion which is subjected to finite frequency effect will be 0.4%–0.8% higher between 20 and 40 s than that after suppressing the finite frequency effect. This is mainly due to the fact that surface waves from the earthquakes used in this study, which are mainly located to the east and south of our array (Figure A2a), sample faster structure in southern China and Sichuan basin (Figure A2b) where the crust is much shallower than in the Tibetan plateau area. We also notice that at $T > 50$ s their differences are very small (~0.1% or less). This is primarily due to the smoothness of upper mantle structure in the global model by *Shapiro and Ritzwoller* [2002], although phase velocity measurements at longer periods are more influenced by finite frequency effect. Hopefully through our approach of suppressing finite frequency effect on the dispersion measurements, we can mitigate the effect of crustal structure outside the array

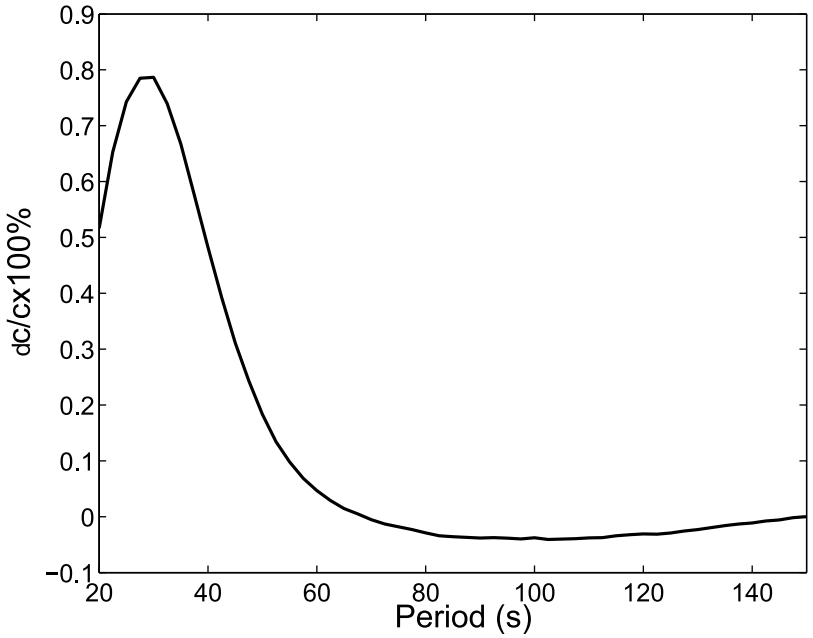

Figure A3. Average difference between the original interstation phase velocity measurements from TS analysis in SE Tibet and those after suppressing the finite frequency effect using equation (A6). The average phase velocities between 20 and 40 s is about 0.5%–0.8% larger before suppressing the finite frequency effect due to the fast structure (thinner crust and high shear wave speed) to the east and south of the array.

area on the inversion of phase velocity maps at intermediate periods.

Appendix B: Point-Wise Shear Wave Velocity Models in SE Tibet

[61] After two-step inversion described in section 4, we obtain 1-D shear wave velocity and azimuthal anisotropy model for every grid point in the study region. Figure B1 shows three examples of the final model at the location (93°, 30°) in the Lhasa Block, (100. 5°, 29°) in the Songpan-Ganze Fold Belt, and (103°, 26°) in the Xiaojiang fault zone of Yangtze Block. The global reference model is shown as the red dashed line with the crust part averaged approximately from the Global Crust 2.0 model (http://igppweb.ucsd.edu/~gabi/crust2.html) and the upper mantle part from the global *ak135* model [*Kennett et al.*, 1995]. For each location, the reference crust shear velocity linearly increases from 3.4 km/s at the surface to 3.85 km/s at the Moho depth, which is a modified version of the three layer crustal model inferred from the Crust 2.0 model with crustal thickness varying from 45 to 70 km. The reason that we did not use the average shear velocity model in the study region as the reference is because the average shear wave velocity in the middle and lower crust in SE Tibet is significantly slower than that of the global average. We observe apparent low velocity layer in the middle-lower crust (20–50 km) of SE Tibet with shear wave speed even slower than 3.3 km/s, which is about 10%–15% slower than the global average, typically 3.6–3.9 km/s at this depth range. We also observe that the azimuthal anisotropy, as shown in the three examples, has large radial variation in both amplitude and azimuth of fast polarization axis. This implies that different depth ranges in the lithosphere of SE Tibet, such as crust and uppermost mantle, may deform differently.

Appendix C: Spatial Smoothing of the Observed Shear Wave Splitting Data

[62] The observed shear wave splitting measurements (red bars in Figure 12 or Figure C1) by *Lev et al.* [2006], *Sol et al.* [2007], and *Wang et al.* [2008] reveal variations in orientation over length scales that are much shorter than the scale of horizontal resolution (about 200 km) from our tomographic inversions (Figures 6 and 8). In order to compare azimuthal anisotropy from both shear wave splitting and from surface wave tomography on a similar length scale, we need to smooth the observed shear wave splitting data to a similar length scale of the tomographic maps for azimuthal anisotropy.

[63] Here we adopt a Gaussian spatial smoothing function to each component of azimuthal anisotropy as we also used for tomographic inversions in section 3 for smoothing the shear wave splitting data. It is expressed as

$$G(M_i, M_j) = \exp\{-0.5d(M_i, M_j)/L^2\}, \qquad \text{(C1)}$$

where M_i and M_j are the two locations in the study region where we have splitting measurements, $d(M_i, M_j)$ is the

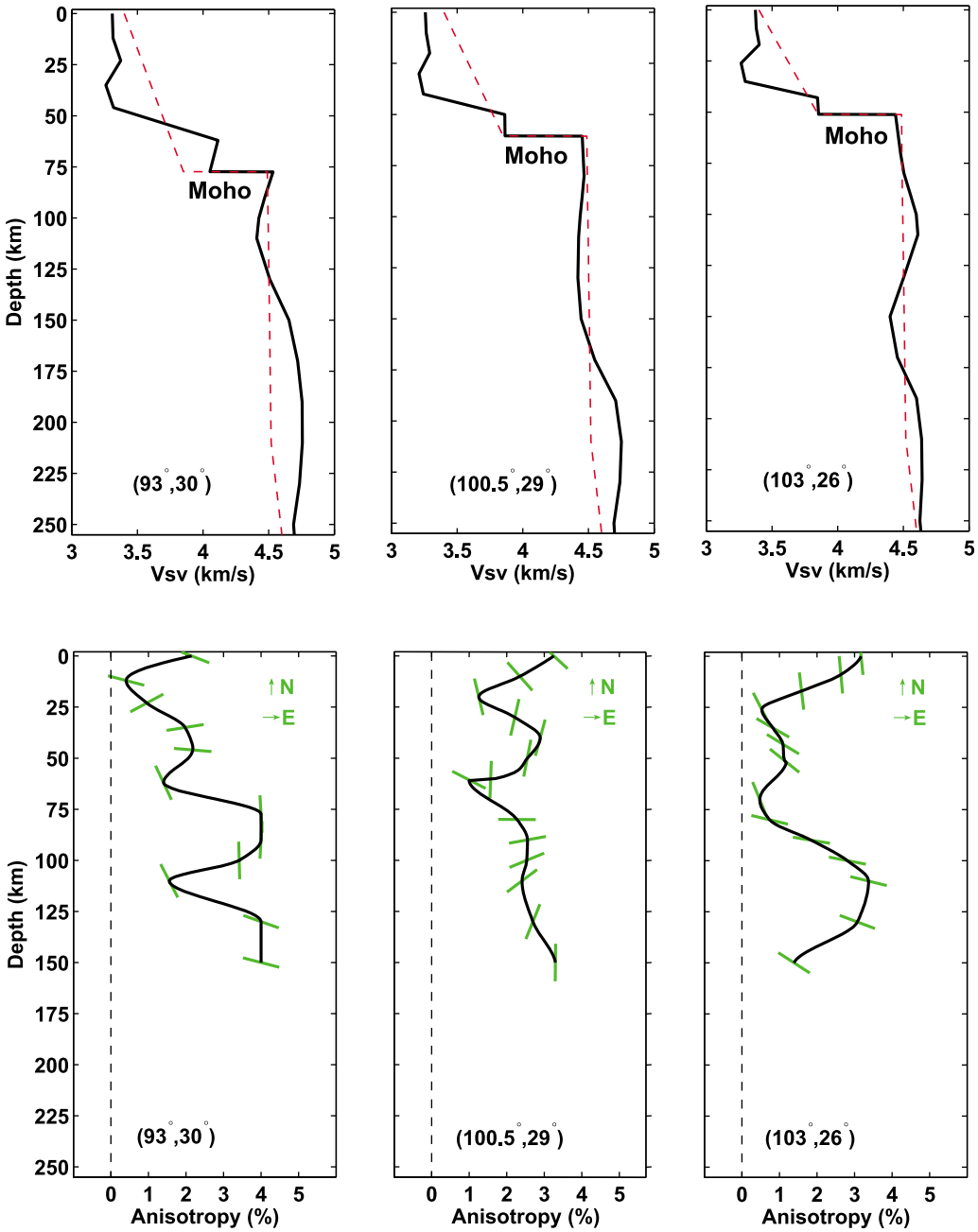

Figure B1. Shear velocity models at three locations in the study region. The top three plots show the vertically polarized shear wave velocity (V_{SV}) model (black line) and the reference model (dashed red line) for plotting the perturbation of V_{SV} in Figure 10. The bottom three plots show the variation of azimuthal anisotropy of V_{SV}, in which the black line gives the magnitude of shear wave azimuthal anisotropy and the orientation of green bars gives the azimuth of the fast polarization axis (north pointing upward and east pointing eastward shown as the arrows in each plot).

distance between these two locations, and L is the spatial smoothing length. Let N denote the total number of splitting measurements, $\delta \boldsymbol{t}$ as the vector of splitting time, and ψ as the vector of angle of fast direction. Since the splitting time and fast direction essentially represent the shear velocity azimuthal anisotropy at some particular location, the splitting intensity function with respect to azimuth φ for vertically polarized shear waves (e.g., equation (4)) for each measurement is defined as

$$s_i(\varphi) = \delta t_i \cos(2(\varphi - \psi_i)) = (\delta t_i \cos 2\psi_i) \cos 2\varphi + (\delta t_i \sin 2\psi_i) \sin 2\varphi. \quad \text{(C2)}$$

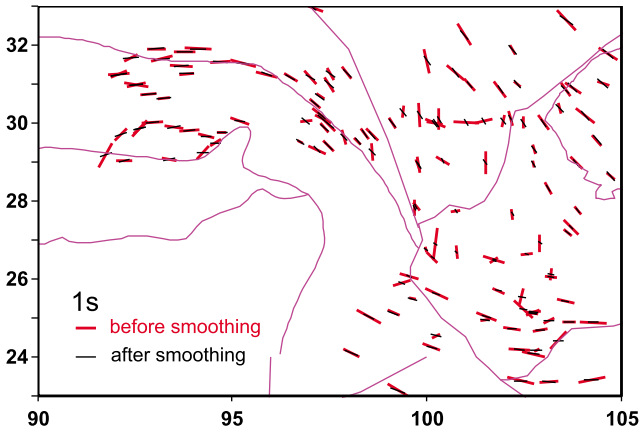

Figure C1. Shear wave splitting measurements [from *Lev et al.*, 2006; *Sol et al.*, 2007; *Wang et al.*, 2008] before and after spatial smoothing as described in Appendix C. The original and smoothed shear wave splitting data are shown as red thick bars and thin black bars, respectively.

For each location with splitting measurement, the smoothed splitting time function is defined as

$$\begin{aligned}\hat{s}_i(\varphi) &= \sum_{k=1}^{N} g_{ik}\delta t_k \cos(2(\varphi-\psi_k)) \\ &= \left\{\sum_{k=1}^{N}(g_{ik}\delta t_k \cos 2\psi_k)\right\}\cos 2\varphi \\ &\quad + \left\{\sum_{k=1}^{N}(g_{ik}\delta t_k \sin 2\psi_k)\right\}\sin 2\varphi, \end{aligned} \tag{C3}$$

where g_{ik} is the normalized Gaussian smoothing coefficient given by

$$g_{ik} = G(M_i, M_k)\Big/\sum_{j=1}^{N} G(M_i, M_j). \tag{C4}$$

Therefore, the shear wave splitting time and fast direction after spatial smoothing is calculated from the following:

$$\begin{cases} \hat{\delta t_i} = \sqrt{\left\{\sum_{k=1}^{N}(g_{ik}\delta t_k \cos 2\psi_k)\right\}^2 + \left\{\sum_{k=1}^{N}(g_{ik}\delta t_k \sin 2\psi_k)\right\}^2} \\ \hat{\psi}_i = \frac{1}{2}\tan^{-1}\left(\left\{\sum_{k=1}^{N}(g_{ik}\delta t_k \sin 2\psi_k)\right\}\Big/\left\{\sum_{k=1}^{N}(g_{ik}\delta t_k \cos 2\psi_k)\right\}\right). \end{cases} \tag{C5}$$

When $L \to 0$, $g_{ik} \to \delta_{ik}$ (the Kronecker delta function), therefore $\hat{s}_i(\varphi) \to s_i(\varphi)$, $\hat{\delta t_i} \to \delta t_i$, and $\hat{\psi}_i \to \psi_i$. Notice that we did not directly smooth the observed splitting time and fast direction considering their nonlinearity.

[64] The spatial correlation length used from surface wave azimuthal anisotropy inversion is about 200–300 km (section 3) and the spatial resolution for our azimuthal anisotropic maps is about 200 km for most periods less than 100 s (Figure 5). In order to smooth the small wavelength (less than 100 km) variations in the shear wave splitting measurements, we finally choose a spatial smooth length of 150 km in equation (C1). The resulting shear wave splitting measurements after smoothing is shown as the black bars in Figure C1. We notice that after smoothing the shear wave splitting data in SW China generally have a smaller splitting time due to cancellation of different fast directions and an overall NNW–SSE fast direction in Sichuan and nearly E-W fast direction in Yunnan.

[65] **Acknowledgments.** We thank the editor (Robert Nowack), the associate editor, an anonymous reviewer, and Lucy Flesch for their constructive comments which helped to improve our manuscript. We thank Anne Meltzer for sharing (prior to formal release) the data of 50 array stations in southeastern Tibet (Namche Barwa Seismic Experiment) deployed by Lehigh University. This work benefited from discussions with Leigh Royden, Clark Burchfiel (MIT), Paul Tapponnier (Institut de Physique du Globe, Paris), Qiyuan Liu (Institute of Geology, Chinese Earthquake Administration), and Denghai Bai (Institute of Geology and Geophysics, Chinese Academy of Sciences). This work is funded by NSF Continental Dynamics Program NSFEAR 0003571 and Geophysics Program NSFEAR 0910618.

References

Argand, E. (1924), La tectonique de l'asie, *Int. Geol. Cong. Rep. Sess.*, *13*(1), 170–372.

Bai, D., et al. (2010), Crustal deformation of the eastern Tibetan plateau revealed by magnetotelluric imaging, *Nat. Geosci.*, *3*, 358–362, doi:10.1038/ngeo830.

Barruol, G., and D. Mainprice (1993), 3-D seismic velocities calculated from lattice-preferred orientation and reflectivity of a lower crustal section - examples of the Val Sesia Setion (ivrea zone, northern Italy), *Geophys. J. Int.*, *115*(3), 1169–1188.

Beaumont, C., R. A. Jamieson, M. H. Nguyen, and B. Lee (2001), Himalayan tectonics explained by extrusion of a low-viscosity channel coupled to focused surface denudation, *Nature*, *414*, 738–742.

Beaumont, C., R. A. Jamieson, M. H. Nguyen, and S. Medvedev (2004), Crustal channel flow: 1. Numerical models with applications to the tectonics of the Himalayan-Tibetan orogen, *J. Geophys. Res.*, *109*, B06406, doi:10.1029/2003JB002809.

Bendick, R., and L. Flesch (2007), Reconciling lithospheric deformation and lower crustal flow beneath central Tibet, *Geology*, *35*, 895–898.

Burchfiel, B. C., L. H. Royden, R. D. Van der Hilst, B. H. Hager, Z. Chen, R. W. King, C. Li, Y. Lu, H. Yao, and E. Kirby (2008), A geological and geophysical context for the Wenchuan earthquake of 12 May 2008, Sichuan, People's Republic of China, *GSA Today*, *18*(7), doi:10.1130/GSATG18A.1.

Chen, Z., B. C. Burchfiel, Y. Liu, R. W. King, L. H. Royden, W. Tang, E. Wang, J. Zhao, and X. Zhang (2000), Global positioning system measurements from eastern Tibet and their implications for India/Eurasia intercontinental deformation, *J. Geophys. Res.*, *105*(B7), 16,215–16,227, doi:10.1029/2000JB900092.

Chevrot, S. (2006), Finite-frequency vectorial tomography: A new method for high-resolution imaging of upper mantle anisotropy, *Geophys. J. Int.*, *165*, 641–657.

Clark, M., and L. H. Royden (2000), Topographic ooze: Building the eastern margin of Tibet by lower crustal flow, *Geology*, *28*(8), 703–706.

Cook, K. L., and L. H. Royden (2008), The role of crustal strength variations in shaping orogenic plateau, with application to Tibet, *J. Geophys. Res.*, *113*, B08407, doi:10.1029/2007JB005457.

Crampin, S., and S. Chastin (2003), A review of shear wave splitting in the crack-critical crust, *Geophys. J. Int.*, *155*(1), 221–240.

DeCelles, P. G., D. M. Robinson, and G. Zandt (2002), Implications of shortening in the Himalayan-fold-thrust belt for uplift of the Tibetan plateau, *Tectonics*, *21*(6), 1062, doi:10.1029/2001TC001322.

de Hoop, M. V., and R. D. van der Hilst (2005), Reply to comment by F. A. Dahlen and G. Nolet on "On sensitivity kernels for 'wave-equation' transmission tomography," *Geophys. J. Int.*, *163*, 952–955.

de Hoop, M. V., R. D. van der Hilst, and P. Shen (2006), Wave-equation reflection tomography: Annihilators and sensitivity kernels, *Geophys. J. Int.*, *167*, 1332–1352, doi:10.1111/j.1365-246X.2006.03132.x.

England, P., and G. Houseman (1986), Finite strain calculations of continental deformation: 2. Comparison with the India-Asia collision zone, *J. Geophys. Res.*, *91*(B3), 3664–3676, doi:10.1029/JB091iB03p03664.

Flesch, L. M., W. E. Holt, P. G. Silver, M. Stephenson, C.-Y. Wang, and W. W. Chan (2005), Constraining the extent of crust-mantle coupling in central Asia using GPS, geologic, and shear wave splitting data, *Earth Planet. Sci. Lett.*, *238*, 248–268.

Griot, D. A., J. P. Montagner, and P. Tapponnier (1998a), Phase velocity structure from Rayleigh and Love waves in Tibet and its neighboring regions, *J. Geophys. Res.*, *103*(B9), 21,215–21,232, doi:10.1029/98JB00953.

Griot, D. A., J. P. Montagner, and P. Tapponnier (1998b), Confrontation of mantle seismic anisotropy with two extreme models of strain, in Central Asia, *Geophys. Res. Lett.*, *25*(9), 1447–1450, doi:10.1029/98GL00991.

Grujic, F., L. S. Hollister, and R. R. Parrish (2002), Himalayan metamorphic sequence as an orogenic channel; insight from Bhutan, *Earth Planet. Sci. Lett.*, *198*(1–2), 177–191, doi:10.1016/S0012-821X(02)00482-X.

Hodges, K. V., J. M. Hurtado, and K. X. Whipple (2001), Southward extrusion of Tibetan crust and its effect on Himalayan tectonics, *Tectonics*, *20*(6), 799–809, doi:10.1029/2001TC001281.

Holt, W. E. (2000), Correlated crust and mantle strain fields in Tibet, *Geology*, *28*, 67–70.

Hu, J., Y. Su, X. Zhu, and Y. Chen (2005), *S* wave velocity and Poisson's ratio structure of crust in Yunnan and its implication, *Sci. China, Ser. D*, *48*, 210–218.

Hu, S., L. He, and J. Wang (2000), Heat flow in the continental area of China: A new data set, *Earth Planet. Sci. Lett.*, *179*, 407–419.

Huang, J., D. Zhao, and S. Zhang (2002), Lithospheric structure and its relationship to seismic and volcanic activity in southwest China, *J. Geophys. Res.*, *107*(B10), 2255, doi:10.1029/2000JB000137.

Huang, H., H. Yao, and R. D. van der Hilst (2010), Radial anisotropy in the crust of SE Tibet and SW China from ambient noise interferometry, *Geophys. Res. Lett.*, *37*, L21310, doi:10.1029/2010GL044981.

Huang, J., and D. Zhao (2006), High-resolution mantle tomography of China and surrounding regions, *J. Geophys. Res.*, *111*, B09305, doi:10.1029/2005JB004066.

Huang, R., Z. Wang, S. Pei, and Y. Wang (2009), Crustal ductile flow and its contribution to tectonic stress in Southwest China, *Tectonophysics*, *47*, 476–489.

Hubbard, J., and J. H. Shaw (2008), Uplift of the Longmen Shan and Tibetan plateau, and the 2008 Wenchuan (M = 7.9) earthquake, *Nature*, *458*, 194–197.

Jordan, T. A., and A. B. Watts (2005), Gravity anomalies, flexure and the elastic thickness structure of the India-Eurasia collisonal system, *Earth Planet. Sci. Lett.*, *236*, 732–750, doi:10.1016/j.epsl.2005.05.036.

Karato, S., H. Jung, I. Katayama, and P. A. Skemer (2008), Geodynamic significance of seismic anisotropy of the upper mantle: New insights from laboratory studies, *Annu. Rev. Earth Planet. Sci.*, *36*, 59–95.

Kennett, B. L. N., E. R. Engdahl, and R. Buland (1995), Constraints on the velocity structure in the earth from travel times, *Geophys. J. Int.*, *122*, 108–124.

King, J., N. Harris, T. Argles, R. Parrish, B. Charlier, S. Sherlock, and H. F. Zhang (2007), First field evidence of southward ductile flow of Asian crust beneath southern Tibet, *Geology*, *35*, 727–730.

Lev, E., M. Long, and R. D. van der Hilst (2006), Seismic anisotropy in eastern Tibet from shear wave splitting reveals changes in lithosphere deformation, *Earth Planet. Sci. Lett.*, *251*, 293–304.

Lévêque, J. J., L. Rivera, and G. Wittlinger (1993), On the use of the checkerboard test to assess the resolution of tomographic inversions, *Geophy. J. Int.*, *115*, 313–318.

Li, C., R. D. van der Hilst, A. S. Meltzer, R. Sun, and E. R. Engdahl (2008), Subduction of the Indian lithosphere beneath the Tibetan plateau and Burma, *Earth Planet. Sci. Lett.*, *274*, 157–168.

Li, C., and R. D. van der Hilst (2010), Structure of the upper mantle and transition zone beneath Southeast Asia from traveltime tomography, *J. Geophys. Res.*, *115*, B07308, doi:10.1029/2009JB006882.

Li, Z. X. (1998), Tectonic history of the major East Asian lithosphere blocks since the mid-Proterozoic, in *Mantle Dynamics and Plate Interactions in East Asia*, edited by M. F. J. Flower et al., *AGU Geod. Ser.*, 27, 211–243.

Li, H., W. Su, C.-Y. Wang, and Z. Huang (2009), Ambient noise Rayleigh wave tomography in western Sichuan and eastern Tibet, *Earth Planet. Sci. Lett.*, *282*, 201–211, doi:10.1016/j.epsl.2009.03.021.

Liu, Q., Y. Li, and J. Chen (2009), Wenchuan M(S)8.0 earthquake: Preliminary study of the *S* wave velocity structure of the crust and upper mantle, *Chinese J. Geophys.*, *52*, 309–319.

Liu-Zeng, J., et al. (2009), Co-seismic ruptures of the 12 May, 2008, Ms 8.0 Wenchuan earthquake, Sichuan: East-West crustal shortening on oblique, parallel thrusts along the eastern edge of Tibet, *Earth Planet. Sci. Lett.*, *286*, 355–370, doi:10.1016/j.epsl.2009.07.017.

Lloyd, G., R. Butler, M. Casey, and D. Mainprice (2009), Mica, deformation fabrics and the seismic properties of the continental crust, *Earth Planet. Sci. Lett.*, *288*, 320–328, doi:10.1016/j.epsl.2009.09.035.

Long, M. L., M. V. de Hoop, and R. D. van der Hilst (2008), Wave-equation shear wave splitting tomography, *Geophys. J. Int.*, *172*, 311–330.

Molnar, P., P. England, and J. Martinod (1993), Mantle dynamics, uplift of the Tibetan plateau, the Indian Monsoon, *Rev. Geophys.*, *31*, 357–396.

Montagner, J.-P. (1986), Regional three-dimensional structures using long period surface waves, *Ann. Geophys.*, *4*, 283–294.

Montagner, J.-P., and H.-C. Nataf (1986), A simple method for inverting the azimuthal anisotropy of surface waves, *J. Geophys. Res.*, *91*(B1), 511–520, doi:10.1029/JB091iB01p00511.

Montagner, J.-P., D.-A. Griot-Pommera, and J. Lavé (2000), How to relate body wave and surface wave anisotropy?, *J. Geophys. Res.*, *105*(B8), 19,015–19,027, doi:10.1029/2000JB900015.

Nelson, K. D., et al. (1996), Partially molten middle crust beneath southern Tibet: Synthesis of Project INDEPTH results, *Science*, *294*, 1684–1688.

Ni, J. F., M. Guzman-Speziale, M. Bevis, W. E. Holt, T. C. Wallace, and W. Seager (1989), Accretionary tectonics of Burma and the three-dimensional geometry of the Burma subduction zone, *Geology*, *17*, 68–71.

Ozacar, A. A., and G. Zandt (2004), Crustal seismic anisotropy in central Tibet: Implications for deformational style and flow in the crust, *Geophys. Res. Lett.*, *31*, L23601, doi:10.1029/2004GL021096.

Percival, J., D. Fountain, and M. Salisbury (1992), Exposed crustal cross sections as windows on the lower crust, in *Continental Lower Crust*, edited by D. Fountain, R. Arculus, and R. Kay, pp. 317–363, Elsevier, Amsterdam.

Priestley, K., J. Jackson, and D. McKenzie (2008), Lithospheric structure and deep earthquakes beneath India, the Himalaya and southern Tibet, *Geophys. J. Int.*, *172*, 345–362, doi:10.1111/j.1365-246X.2007.03636.x.

Replumaz, A., H. Karason, R. D. van der Hilst, J. Besse, and P. Tapponnier (2004), 4-D evolution of SE Asia's mantle from geological reconstructions and seismic tomography, *Earth Planet. Sci. Lett.*, *221*, 103–115, doi:10.1016/S0012-821X(04)00070-6.

Rippe, D., and M. Unsworth (2010), Quantifying crustal flow in Tibet with magnetotelluric data, *Phys. Earth Planet. Int.*, *179*, 107–121, doi:10.1016/j.pepi.2010.01.009.

Royden, L. H., B. C. Burchfiel, R. W. King, E. Wang, Z. Chen, F. Shen, and Y. Liu (1997), Surface deformation and lower crustal flow in eastern Tibet, *Science*, *276*, 788–790.

Royden, L. H., B. K. Burchfiel, and R. D. van der Hilst (2008), The geological evolution of the Tibetan plateau, *Science*, *321*, 1054–1058.

Sambridge, M. (1999a), Geophysical inversion with a neighbourhood algorithm: I. Searching a parameter space, *Geophys. J. Int.*, *138*, 479–494.

Sambridge, M. (1999b), Geophysical inversion with a neighbourhood algorithm: II. Appraising the ensemble, *Geophys. J. Int.*, *138*, 727–746.

Savage, M. K. (1999), Seismic anisotropy and mantle deformation: What have we learned from shear wave splitting? *Rev. Geophys.*, *37*, 65–106.

Sieminski, A., H. Paulssen, and J. Trampert (2008), Finite-frequency SKS splitting: Measurement and sensitivity kernels, *Bull. Seismol. Soc. Am.*, *98*, 1797–1810, doi:10.1785/0120070297.

Shapiro, N. M., and M. H. Ritzwoller (2002), Monte-Carlo inversion for a global shear-velocity model of the crust and upper mantle, *Geophys. J. Int.*, *151*(1), 88–105.

Shapiro, N. M., M. H. Ritzwoller, P. Molnar, and V. Levin (2004), Thinning and flow of Tibetan crust constrained by seismic anisotropy, *Science*, *35*, 233–236.

Shen, F., L. H. Royden, and B. C. Burchfiel (2001), Large-scale crustal deformation of the Tibetan plateau, *J. Geophys. Res.*, *106*(B4), 6793–6816, doi:10.1029/2000JB900389.

Shen, Z.-K., J. Lü, M. Wang, and R. Bürgmann (2005), Contemporary crustal deformation around the southeast borderland of the Tibetan plateau, *J. Geophys. Res.*, *110*, B11409, doi:10.1029/2004JB003421.

Simons, F. J., R. D. van der Hilst, J. P. Montagner, and A. Zielhuis (2002), Multimode Rayleigh wave inversion for heterogeneity and azimuthal anisotropy of the Australian upper mantle, *Geophys. J. Int.*, *151*(3), 738–754.

Smith, M. L., and F. A. Dahlen (1973), Azimuthal dependence of Love and Rayleigh wave propagation in a slightly anisotropic medium, *J. Geophys. Res.*, *78*(17), 3321–3333, doi:10.1029/JB078i017p03321.

Sol, S., et al. (2007), Geodynamics of southeastern Tibet from seismic anisotropy and geodesy, *Geology*, *35*, 563–566, doi:10.1130/G23408A.1.

Tapponnier, P., G. Peltzer, A. Y. Le Dain, R. Armijo, and P. Cobbold (1982), Propagating extrusion tectonics in Asia: New insights from simple experiments with plasticine, *Geology*, *10*, 611–616.

Tapponnier, P., Z. Xu, F. Roger, B. Meyer, N. Arnaud, G. Wittlinger, and J. Yang (2001), Oblique stepwise and growth of the Tibet plateau, *Science*, *294*, 1671–1677.

Tarantola, A., and B. Valette (1982), Generalized nonlinear inverse problem solved using the least squares criterion, *Rev. Geophys. Space Phys.*, *20*(2), 219–232.

Unsworth, M. J., A. G. Jones, W. Wei, G. Marquis, S. G. Gokarn, and J. E. Spratt (2005), Crustal rheology of the Himalaya and southern Tibet from magnetotelluric data, *Nature*, *438*, 78–81.

van der Hilst, R. D., E. R. Engdahl, and W. Spakman (1993), Tomographic inversion of P and pP data for aspherical mantle structure below the northwest Pacific region, *Geophys. J. Int.*, *115*, 264–302.

Wang, C.-Y., W. Chan, and W. Mooney (2003), Three-dimensional velocity structure of crust and upper mantle in southwestern China and its tectonic implications, *J. Geophys. Res.*, *108*(B9), 2442, doi:10.1029/2002JB001973.

Wang, C.-Y., L. M. Flesch, P. G. Silver, L.-J. Chang, and W. W. Chan (2008), Evidence for mechanically coupled lithosphere in central Asia and resulting implication, *Geology*, *36*, 363–366, doi:10.1130/G24450A.1.

Wang, C.-Y., H. Lou, P. G. Silver, L. Zhu, and L. Chang (2010), Crustal structure variation along 30°N in the eastern Tibetan plateau and its tectonic implications, *Earth Planet. Sci. Lett.*, *289*, 367–376, doi:10.1016/j.epsl.2009.11.026.

Wang, E., B. C. Burchfiel, L. H. Royden, L. Chen, J. Chen, W. Li, and Z. Chen (1998), Late Cenozoic Xianshuihe-Xiaojiang, Red River and Dali fault systems of southwestern Sichuan and central Yunnan, China, *Spec. Pap. Geol. Soc. Am.*, *327*, 1–108.

Wang, E., and B. C. Burchfiel (2000), Late Cenozoic to Holocene deformation in southwestern Sichuan and adjacent Yunnan, China, and its role in formation of the southeastern part of the Tibetan plateau, *Geol. Soc. Am. Bull.*, *112*, 413–423.

Wei, W., et al. (2001), Detection of widespread fluids in the Tibetan crust by magnetotelluric studies, *Science*, *292*(5517), 716–719.

Weiss, T., S. Siegesmund, W. Rabbel, T. Bohlen, and M. Pohl (1999), Seismic velocities andanisotropy of the lower continental crust: A review, *Pure Appl. Geophys.*, *156*, 97–122.

Xu, L., S. Rondenay, and R. D. van der Hilst (2007), Structure of the crust beneath the Southeastern Tibetan plateau from teleseismic receiver functions, *Phys. Earth Planet. Int.*, *165*, 176–193, doi:10.1016/j.pepi.2007.09.002.

Yao, H., R. D. van der Hilst, and M. V. de Hoop (2006), Surface wave array tomography in SE Tibet from ambient seismic noise and two-station analysis: I. Phase velocity maps, *Geophys. J. Int.*, *166*, 732–744.

Yao, H., C. Beghein, and R. D. van der Hist (2008), Surface wave array tomography in SE Tibet from ambient seismic noise and two-station analysis: II. Crustal and upper-mantle structure, *Geophys. J. Int.*, *163*, 205–219, doi:10.1111/j.1365-246X.2007.03696.x.

Yao, H., X. Campman, M. V. de Hoop, and R. D. van der Hilst (2009), Estimation of surface wave Green's function from correlations of direct waves, coda waves, and ambient noise in SE Tibet, *Phys. Earth Planet. Inter.*, *177*, 1–11, doi:10.1016/j.pepi.2009.07.002.

Yao, H., and R. D. van der Hilst (2009), Analysis of ambient noise energy distribution and phase velocity bias in ambient noise tomography, with application to SE Tibet, *Geophys. J. Int.*, *179*, 1113–1132, doi:10.1111/j.1365-246X.2009.04329.x.

Yi, G., H. Yao, J. Zhu, and R. D. van der Hilst (2010), Lithospheric deformation of continental China from Rayleigh wave azimuthal anisotropy, *Chinese J. Geophys.*, *53*, 256–268, doi:10.3969/j.issn.0001-5733.2010.02.004.

Yin, A., and T. M. Harrison (2000), Geologic evolution of the Himalayan-Tibetan orogen, *Annu. Rev. Earth Planet. Sci.*, *28*, 211–280.

Zhang, P., et al. (2004), Continuous deformation of the Tibetan plateau from global positioning system data, *Geology*, *32*(9), 809–812.

Zhang, Z., Y. Wang, Y. Chen, G. A. Houseman, X. Tian, E. Wang, and J. Teng (2009), Crustal structure across Longmenshan fault belt from passive source seismic profiling, *Geophys. Res. Lett.*, *36*, L17310, doi:10.1029/2009GL039580.

Zhao, W., and W. J. Morgan (1987), Injection of Indian crust into Tibetan lower crust: A two dimensional finite element model study, *Tectonics*, *64*(4), 489–504, doi:10.1029/TC006i004p00489.

Zhou, Y., F. A. Dahlen, and G. Nolet (2004), Three-dimensional sensitivity kernels for surface wave observables, *Geophys. J. Int.*, *158*, 142–168.

Zurek, B., A. Meltzer, S. Sol, X. Zhang, and J. Zhang (2005), Measurements of crustal thickness and Poisson's ratio in southeastern Tibet from receiver functions, *Eos Trans. AGU*, *86*(52), Fall Meet. Suppl., Abstract T41A–1283.

J.-P. Montagner, Seismology Laboratory, Institut de Physique du Globe de Paris, 75238 Paris Cedex 05, France.

R. D. van der Hilst, Department of Earth, Atmospheric, and Planetary Sciences, Massachusetts Institute of Technology, Cambridge, MA 02139, USA.

H. Yao, Institute of Geophysics and Planetary Physics, Scripps Institution of Oceanography, University of California, San Diego, 9500 Gilman Dr., La Jolla, CA 92093-0225, USA. (hjyao@mit.edu)